Review of Scientific Instruments

Invited Article: Advances in tunable laser-based radiometric calibration applications at the National Institute of Standards and Technology, USA

Cite as: Rev. Sci. Instrum. **89**, 091301 (2018); https://doi.org/10.1063/1.5004810
Submitted: 15 September 2017 . Accepted: 25 August 2018 . Published Online: 26 September 2018

John T. Woodward, Ping-Shine Shaw, Howard W. Yoon, Yuqin Zong, Steven W. Brown, and Keith R. Lykke

REVIEW OF SCIENTIFIC INSTRUMENTS **89**, 091301 (2018)

Invited Article: Advances in tunable laser-based radiometric calibration applications at the National Institute of Standards and Technology, USA

John T. Woodward, Ping-Shine Shaw, Howard W. Yoon, Yuqin Zong, Steven W. Brown, and Keith R. Lykke
National Institute of Standards and Technology, 100 Bureau Drive, Gaithersburg, Maryland 20899, USA

(Received 15 September 2017; accepted 25 August 2018; published online 26 September 2018)

Recent developments at the National Institute of Standards and Technology's facility for Spectral Irradiance and Radiance responsivity Calibrations using Uniform Sources (SIRCUS) are presented. The facility is predicated on the use of broadly tunable narrow-band lasers as light sources in two key radiometric calibration applications. In the first application, the tunable lasers are used to calibrate the spectral power responsivities of primary standard detectors against an absolute cryogenic radiometer (ACR). The second function is to calibrate the absolute radiance and irradiance responsivities of detectors with uniform light sources, typically generated by coupling the laser light into integrating spheres. The radiant flux from the uniform sources is determined by the ACR-calibrated primary standard detectors. Together these sources and detectors are used to transfer radiometric scales to a variety of optical instruments with low uncertainties. We describe methods for obtaining the stable, uniform light sources required for low uncertainty measurements along with advances in laser sources that facilitate tuning over broader wavelength ranges. Example applications include the development of a detector-based thermodynamic temperature scale, the calibration and characterization of spectrographs, and the use of a traveling version of SIRCUS (T-SIRCUS) to calibrate large aperture Earth observing instruments and astronomical telescopes. https://doi.org/10.1063/1.5004810

I. INTRODUCTION

Due to their high power, low wavelength uncertainty, and narrow bandwidth, tunable laser systems have been used since the early 1980s as the source of radiant flux to calibrate a wide variety of instruments that measure light. Instruments used in derivations of fundamental radiometric and photometric quantities such as irradiance, radiance temperature, and candela have been calibrated using tunable laser sources. In the NIST Spectral Irradiance and Radiance responsivity Calibrations using Uniform Sources (SIRCUS) facility, broadly tunable, computer-controlled lasers have been developed to cover the spectral range from 210 nm to 2500 nm with high power and narrow bandwidth.[1]

At NIST, traceability for optical power responsivity is to the Primary Optical Watt Radiometer (POWR),[2] an absolute cryogenic radiometer and the nation's standard for optical power. The SIRCUS laser systems are used to perform the optical power responsivity comparison between POWR and transfer standard detectors. As an absolute cryogenic radiometer, POWR provides traceability to the International System of Units (SI) by comparison to traceable electrical power measurements. Adding a precision aperture to the transfer standard detector gives a standard detector for irradiance responsivity. The area of the aperture can be determined traceably to the SI (the meter) using the NIST Aperture Measurement Facility.[3] These standard detectors are used with SIRCUS to maintain and disseminate low-uncertainty scales of radiance-, irradiance-, and power-responsivity over the spectral range from 210 nm to 2500 nm.

Supplementing the use of SIRCUS for radiometric calibration is the closely related topic of radiometric characterization. The high power and narrow line width of the SIRCUS laser systems have been used to characterize stray and scattered light (SL) in spectrographs and other optical systems and allow for measurements over a large dynamic range. While not calibration in the strict sense, these characterization measurements greatly improve the understanding of the measurements made with complex optical instruments and are necessary for the development of an accurate uncertainty budget. Sensor characterization is an increasing focus of the work done on SIRCUS and characterization themes are included in the applications presented below.

In Sec. II, the general layout of NIST's laser-based SIRCUS calibration facility is described along with the detector standards that hold the irradiance responsivity scale over the spectral region from 210 nm to 2500 nm. In Sec. III, the measurement equation is presented assuming an ideal light source, developments in tunable laser systems used on SIRCUS are discussed, and typical uncertainty budgets are given. Section IV introduces SIRCUS-based calibrations with applications related to primary radiometric standards and units. Section V gives several example applications of the SIRCUS and T-SIRCUS facilities and systems. Conclusions are provided in Sec. VI.

II. NIST FACILITY FOR SPECTRAL IRRADIANCE AND RADIANCE RESPONSIVITY CALIBRATIONS USING UNIFORM SOURCES (SIRCUS)

Figure 1 is a schematic diagram of NIST's SIRCUS facility.[1] In SIRCUS, the output of a high power, tunable laser is first directed through an intensity stabilizer that controls the

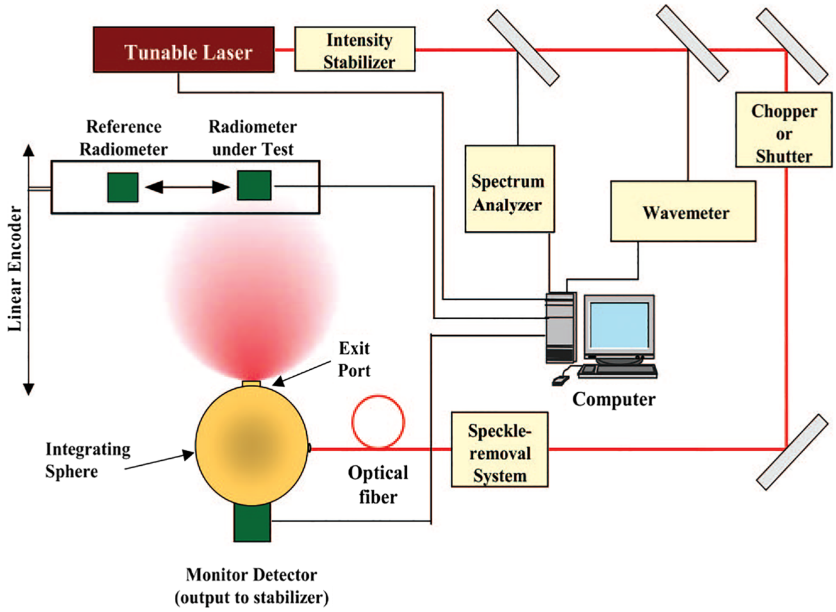

FIG. 1. Schematic diagram of NIST's SIRCUS setup. Reprinted with permission from Brown *et al.*, Appl. Opt. **45**, 8218 (2006). Copyright 2006 The Optical Society.

relative optical power in the beam to better than 0.1% of the set point. A portion of the laser beam is sent into a wavemeter that measures the wavelength of the radiation to within 0.001 nm, and occasionally, a beamsplitter sends another portion of the laser beam into a spectrum analyzer to measure the bandwidth and mode stability of the laser. A shutter and/or chopper is placed in the beam path before the light is coupled to an optical fiber. Typically, a multi-mode optical fiber is used to deliver the radiant flux from the laser table into the calibration source, in this case an integrating sphere source (ISS). Methods used to reduce the effect of laser speckle in the sphere caused by the coherence of the laser beam are discussed below.

For most calibrations, sources and detectors are located inside a light-tight box that has been covered on the inside with Ultrapol™,[4] a material with excellent light-absorbing properties: the measured reflectance is on the order of 0.1% to 0.3% from 300 nm to 2.5 μm.[104] Baffles are often installed between the source and the detectors to minimize effects of scattered radiation on the measurement. SIRCUS can be set up in either of two equivalent configurations with either the source or the detectors mounted on a motorized three-axis stage with position encoders and the other in a fixed position on a bench with a tip-tilt stage for alignment. For ease of discussion, we will assume the source is on the stage. A computer controls the stage motion, tunes the laser wavelength, and records the outputs of the detectors, wavemeter, ISS monitor, and other instruments.

The availability of tunable lasers defines the spectral coverage possible on SIRCUS, while the quality of the reference standard detectors and their uncertainties ultimately establish the calibration uncertainties achievable. Also important to remember, but generally not a limiting factor, is that the optical properties of some components limit their useful wavelength range, so, for example, different optical fibers are used in the UV and the IR. In Sec. II A, we discuss the optical sources; in Sec. II B, the discussion is focused on the transfer standard detectors; and in Sec. II C, the choice of optical fibers is presented.

A. Sources

Different optical fiber-fed sources are used, depending on the details of the radiometric calibration; in most calibrations, integrating sphere sources (ISS) are used. Small-diameter integrating spheres—with diameters ranging from 2.54 cm to 5.08 cm—equipped with precision apertures with diameters ranging from 3 mm to 8 mm are typically used for irradiance responsivity calibrations. Larger diameter spheres—30 cm diameter—with 5 cm to 10 cm diameter exit ports are used for radiance responsivity calibrations of smaller instruments. Still larger ISSs, up to 1 m in diameter, are used to calibrate large aperture instruments such as NASA sensors designed to be used in space. The interiors of the spheres are made of a sintered polytetrafluoroethylene-based (PTFE-based) or a barium sulfate-based coating; both of which have high diffuse reflectance from about 250 nm to 2500 nm. For the larger area ISS, the irradiance when illuminated by the SIRCUS lasers is uniform to within a tenth of a percent over several cm at a 1 m separation from the integrating sphere. Similarly, the radiance from the integrating sphere is typically uniform to within a few tenths of a percent over the central 90% of the exit aperture, as shown in Fig. 2. Typical irradiance levels at 1 m using a 2.54 cm diameter integrating sphere with a 5 mm diameter aperture range from approximately 1 μW/cm^2 to 10 μW/cm^2, depending on the wavelength. Radiance levels between 1 mW/cm^2/sr and 5 mW/cm^2/sr are standard for a 30 cm diameter sphere with a 7.5 cm diameter output port.

Integrating spheres may fluoresce when irradiated by a blue or UV laser beam, which can result in a significant calibration error, especially when calibrating photometers and filter radiometers.[5,6] Therefore, it is critical that the fluorescence of the integrating sphere is tested and evaluated before calibrations at shorter wavelengths. A spectrometer with a known relative spectral response can be used to measure the sphere output and obtain the ratio of the radiance from the fluorescence to the excitation wavelength. Note that depending on the relative response of the Device Under Test (DUT), even low

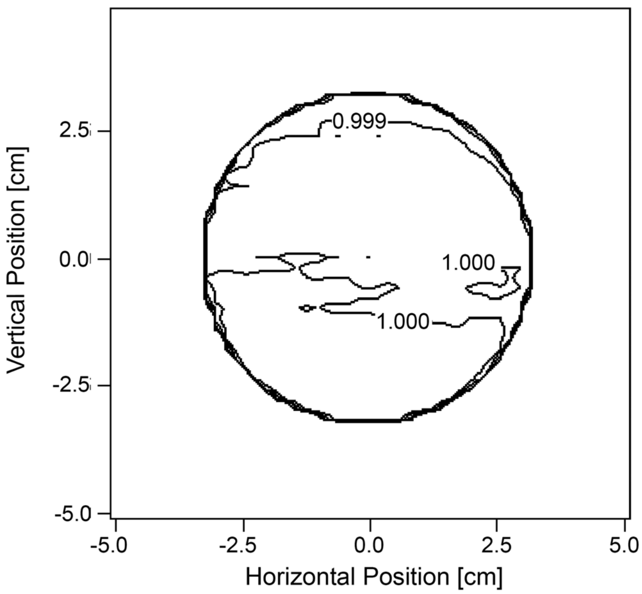

FIG. 2. Radiance scan across an 8 mm diameter aperture on a 30 cm sphere used in the calibration of radiation thermometers.

fluorescence levels can yield significant errors if the DUT is more sensitive to the fluorescence wavelengths.

High intensity, quasi-collimated light sources can be obtained using a mirror-based collimator. Mirrors have the advantage over lenses of achromaticity from the UV to the IR. In addition to the collimators in SIRCUS, both on- and off-axis collimator sources have been developed in collaboration with NASA[7] and the United States Geological Survey (USGS)[8] for the characterization and calibration of large aperture telescopes. Non-uniformities of 1% or less are achieved over a 5 cm diameter area with an irradiance 2 orders of magnitude greater than values achievable with the integrating sphere alone.

B. Transfer standard detectors

The scales of all standard reference detectors used at SIRCUS are directly derived against a cryogenic radiometer, either the Primary Optical Watt Radiometer (POWR)[2,9] or a transfer cryogenic radiometer,[1] using SIRCUS lasers. POWR is a state-of-the-art liquid helium-cooled radiometer designed to achieve the lowest possible uncertainties and is currently the US national standard for optical power. The power responsivity is readily converted into irradiance or radiance responsivity by the addition of precision apertures with accurately measured areas.[1,3]

Transfer standard detectors used in the SIRCUS facility have several different configurations, among them (1) tunnel-trap detectors, (2) reflectance trap detectors, (3) integrating sphere-based standards, and (4) single element photodiodes. Figure 3 shows the power responsivities of four types of reference standard detectors maintained in SIRCUS to cover calibrations ranging from 210 nm to 2500 nm. There are significant overlaps in spectral regions between neighboring reference standard detectors to ensure a smooth and reliable transition of a radiometric scale from one detector region to another.

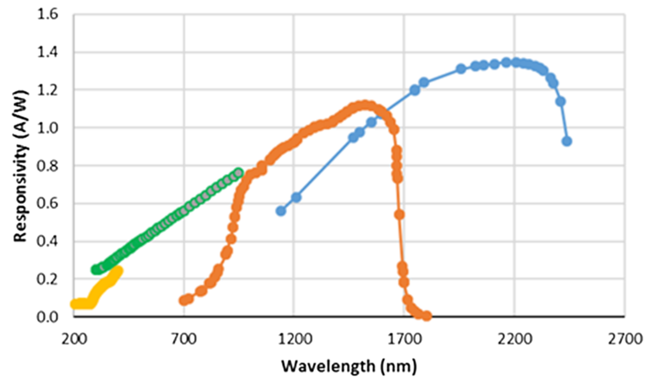

FIG. 3. The spectral responsivity of SIRCUS working standards, a UV working standard (yellow), a VisNIR Si tunnel trap detector (green), an InGaAs working standard (orange), and an extended InGaAs working standard (blue).

A particular property of the trap detector, both the reflectance and tunnel configuration, is that the incident light is almost completely absorbed by the photodiodes in the trap detector.[10,11] In this case, the external quantum efficiency (EQE), defined as the number of electrons that flow through the external circuitry from the detector induced by each incident photon, approaches that of the internal quantum efficiency (IQE) or the number of electrons excited by each absorbed photon. A silicon photodiode's IQE in the visible range is very close to 1. The IQE has been modeled,[12] based on the material properties of silicon and the diode configuration of a silicon photodiode. Figure 4 shows the EQE's of 4 different tunnel trap working standards. Note that the EQEs of 3 of the 4 detectors agree extremely well with each other, and the EQEs of all 4 detectors agree to within approximately 0.2% from 940 nm to 405 nm and within 0.5% from 405 nm to 350 nm.

Standard reflectance trap configurations commonly use either 3 or 4 detectors. For the 4-detector reflectance trap configuration,[11] the photodiodes are arranged in a way to subject incoming light to seven reflections before it exits back out of the entrance aperture. These multiple reflections give two major advantages for trap detectors over single element photodiodes. First, at a typical value of 0.02%, the back

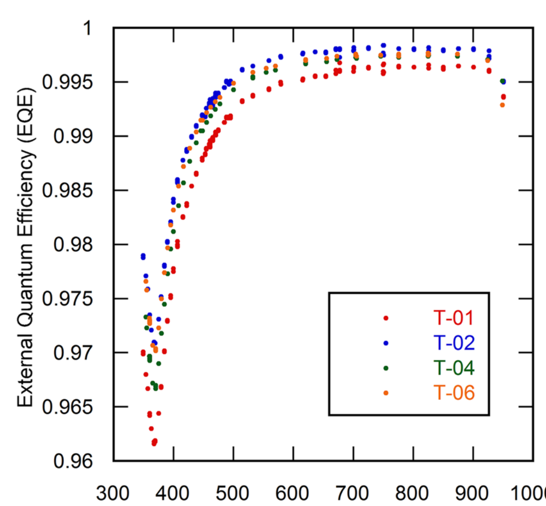

FIG. 4. The EQE of 4 reference standard tunnel trap detectors.

reflection of a trap detector with light reflected from seven surfaces is significantly lower than the reflectance from a single element Si photodiode, which is around 30% in the Si range. Second, because of the low back reflectance of a trap detector, it is insensitive to changes in reflectance by any of the photodiode front surfaces resulting in a better response uniformity and stability. Three-element reflectance trap detectors with silicon photodiodes that have nitrided silicon-oxide passivating layers are used in SIRCUS as transfer standards for wavelengths in the 210 nm to 350 nm range because these nitrided silicon (n-Si) photodiodes have superior UV radiation hardness compared to regular silicon photodiodes.[13]

A variation of the reflectance trap configuration is the tunnel trap configuration where six photodiodes, two medium- and four large-size silicon photodiodes, are tightly packed in a fashion such that incoming light undergoes six reflections before exiting the trap detector along the same direction as the incoming light.[14] This ensures one more reflection than a traditional three-element trap detector, one less reflection than Zalewski and Duda's 4-element trap,[11] and eliminates back-reflected light that can induce errors for some experimental configurations. The silicon detectors in the tunnel traps are non-windowed to avoid fringing effects from the window and are not temperature stabilized. Si shows a temperature dependence to its responsivity beyond 960 nm; consequently, to achieve the lowest uncertainties, the long-wavelength cutoff in the Si tunnel trap devices is limited to approximately 960 nm though silicon has a finite response that extends beyond 1200 nm. Tunnel traps are used as the primary transfer standards in SIRCUS over the spectral range from 300 nm to 960 nm.

Single element Indium Gallium Arsenide (InGaAs) photodiodes are used to hold and disseminate the responsivity scale from approximately 950 nm up to their cutoff wavelength, around 1650 nm. Figure 5 shows the spectral responsivities of InGaAs detectors from 5 different vendors. The detectors are separated into two groups. The first group has a short-wavelength cutoff around 1100 nm, while the second group has a short-wavelength cutoff around 950 nm. The difference in the short-wavelength cutoff is due to the InGaAs detectors having different substrates. These detectors have non-negligible responsivities through the visible.

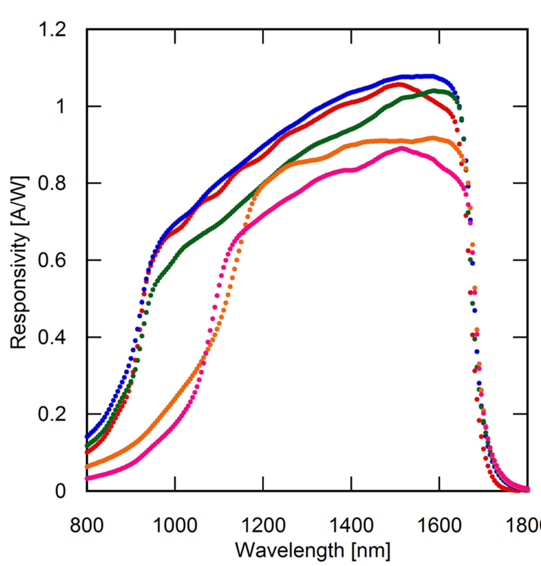

FIG. 5. Spectral responsivities of 5 InGaAs photodetectors from different vendors show large variations between different models.

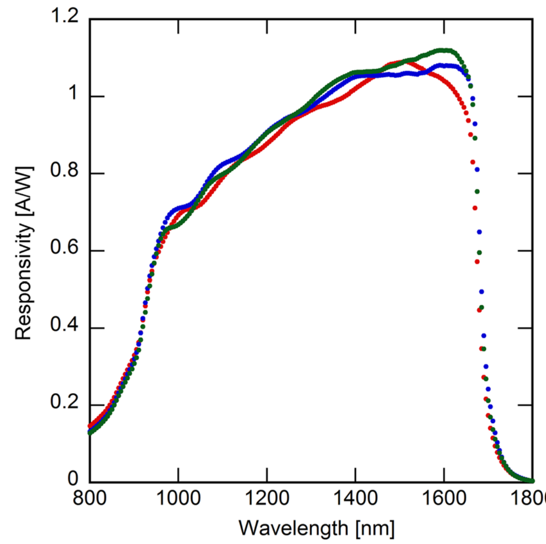

FIG. 6. Spectral responsivities of 4 InGaAs photodetectors from one vendor.

Figure 6 shows the responsivities of 4 InGaAs detectors from the same vendor. The responsivities are very similar for each detector, but differences between detectors are much larger than differences between Si detectors.

InGaAs detectors show negligible temperature-dependence to their responsivity, except near the InGaAs and substrate band edges. Figure 7 shows the temperature dependence of the responsivities of the InGaAs detectors given in Fig. 6. The figure shows a discernable temperature dependence over the range from 20 °C to 30 °C, in the regions around the band-edges, 925 nm on the short-wave side corresponding to

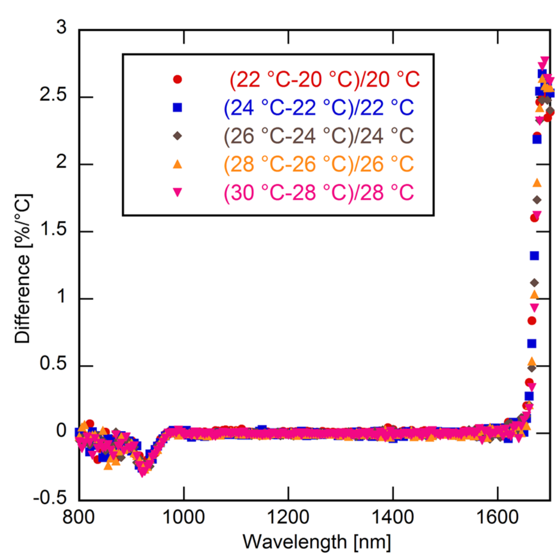

FIG. 7. Temperature dependence of the InGaAs photodetectors' responsivities given in Fig. 6. The detector responsivity was measured different temperature setpoints in 2 °C intervals from 20 °C to 30 °C. The responsivity is stable through much of the wavelength range and shows large, but consistent, changes near the band edges.

the substrate band-edge and 1650 nm for the long-wave side corresponding to the InGaAs band-edge.

Extended InGaAs (ext-InGaAs) photodiodes are currently used as transfer standards for the irradiance scale from 1600 nm to 2500 nm.[15] However, the response uniformity of ext-InGaAs photodiodes across their active area can be poor. To mitigate the higher uncertainty caused by the spatially non-uniform detector response, reference standard detectors were built by mounting ext-InGaAs photodiodes on integrating spheres. By using the integrating sphere as the input optic to diffuse the input light, the dependence of photodiode response on input light spatial distribution is greatly reduced. However, due to the low throughput of the integrating sphere, the radiometer's responsivity is a factor of ~100 less than the single element ext-InGaAs detector.

C. Choice of optical fiber

For certain applications, for example irradiance measurements where the integrating sphere diameter can be 25 mm or less, or in cases where there is insufficient baffling, the calibration of the monitor photodiode can depend on the spatial distribution of the input radiant flux from the optical fiber. Ideally, the spatial far-field distribution of the radiation pattern from an optical fiber would be constant, independent of excitation conditions, like the far-field distribution from a single mode fiber, for example. However, the coupling efficiency into single mode fibers tends to be low and multimode fibers are typically used to transfer laser light from the source to the ISS. Exciting a step index optical fiber with collimated light off-axis results in a circular spatial distribution of the transmitted radiation often called a "doughnut mode." The diameter of the spatial circle is a function of the off-axis excitation angle. By contrast, a sinusoidal spatial pattern propagates in graded-index (GRIN) optical fiber, with the optical radiation constantly re-focusing. As a result, the spatial distribution at the output of a GRIN fiber is not sensitive to the angle of incidence of the input radiation. Mixing the propagating modes in the fiber, either via a mode mixer[16] or by engineered control over the fiber composition[17] can also result in constant far-field distributions. In this example, and other applications where the far-field spatial distribution of the radiation is important, care must be taken over the far-field spatial distribution from the optical fiber.

Also of concern is the transmission efficiency of the fiber. A low-OH silica fiber is used for wavelengths longer than 400 nm. While a high-OH silica fiber has better transmittance in the UV but is poor in the IR. By 2500 nm, even the low-OH silica transmittance is poor and zirconium fluoride is useful going farther into the IR. For all fibers, we prefer a stainless-steel jacketing, as the common plastic jacketing can be transparent at some wavelengths, particularly in the IR. This leads to a light source other than the aperture of the ISS and causes radiometric errors.

III. THE MEASUREMENT EQUATION

All calibrations, whether the radiometric responsivity quantity of interest is radiant power, irradiance or radiance, follow the same basic format: the radiometric unit of interest is transferred to the Device Under Test (DUT) by direct substitution using reference standard transfer radiometers. With this method, a transfer standard radiometer measures the source radiometric quantity, either radiance or irradiance, and a DUT is then placed in front of the source and its signal recorded. Monitor detectors are commonly used to account for any changes in radiant flux between measurements. The laser is blocked and the dark signal is recorded prior to each measurement. The responsivity at a given excitation wavelength is the instrument's net output signal (with the dark signal subtracted from the light signal), corrected by the flux transfer and divided by the radiometric quantity to be measured.

The measurement equation relates the observed signal $S(\lambda)$ from an instrument having a responsivity $R(\lambda)$ to a source radiometric quantity, in this example radiance, $L(\lambda)$. Equation (3.1) gives the general measurement equation, while Eq. (3.2) gives the measurement equation with the SI units attached to each parameter expressed,

$$S(\lambda) = \int R(\lambda)L(\lambda)d\lambda, \tag{3.1}$$

$$S(\lambda)[A] = \int R(\lambda)\left[\mathrm{A}\cdot\mathrm{W}^{-1}\cdot\mathrm{m}^{2}\cdot\mathrm{sr}\right]L(\lambda) \times\left[\mathrm{W}\cdot\mathrm{m}^{-2}\cdot\mathrm{sr}^{-1}\cdot\mathrm{nm}^{-1}\right]d\lambda[\mathrm{nm}]. \tag{3.2}$$

Due to the narrow linewidth of the laser sources in SIRCUS, the spectral radiance of the source can be approximated by a delta function with the laser wavelength given by λ_o, Eq. (3.4),

$$L(\lambda) \cong \delta - \text{function} \Rightarrow L(\lambda)\delta(\lambda-\lambda_o), \tag{3.3}$$

$$L(\lambda) = L(\lambda)\left[\mathrm{W}\cdot\mathrm{m}^{-2}\cdot\mathrm{sr}^{-1}\right]\delta(\lambda-\lambda_o)\left[\mathrm{nm}^{-1}\right]. \tag{3.4}$$

Inserting the equation for radiance given by Eq. (3.4) into Eq. (3.2) gives Eq. (3.5) and applying the delta function leads to the general SIRCUS measurement equation, Eq. (3.6),

$$S(\lambda)[A] = \int R(\lambda)\left[\mathrm{A}\cdot\mathrm{W}^{-1}\cdot\mathrm{m}^{2}\cdot\mathrm{sr}\right]L(\lambda) \times\left[\mathrm{W}\cdot\mathrm{m}^{-2}\cdot\mathrm{sr}^{-1}\right]\delta(\lambda-\lambda_o)\left[\mathrm{nm}^{-1}\right]d\lambda[\mathrm{nm}], \tag{3.5}$$

$$S(\lambda_o)[A] = R(\lambda_o)\left[\mathrm{A}\cdot\mathrm{W}^{-1}\cdot\mathrm{m}^{2}\cdot\mathrm{sr}\right]L(\lambda_o)\left[\mathrm{W}\cdot\mathrm{m}^{-2}\cdot\mathrm{sr}^{-1}\right]. \tag{3.6}$$

In Secs. III A–III F, we discuss experimental design effects on the uncertainty budget. Laser power control, optical fiber, the spatial coherence of the incident laser radiation, which gives rise to speckle, and the observation and possible mitigation of interference fringes, commonly observed in an instrument's measured responsivity using narrow-band lasers, are discussed. In Sec. III F, typical uncertainty budgets are presented.

A. Irradiance measurements

The reference standard transfer detectors used on SIRCUS are irradiance meters. The radiance is determined by measuring the irradiance at a known distance and dividing by the solid angle. In order to determine the solid angles, the areas of the

ISS and transfer standard apertures must be known along with the distance between the detector and source apertures. Consider the typical case where both circular apertures lie along the optical axis.[18,19] Let the radius of the source aperture be r_s, the radius of the detector aperture be r_d, and the distance between the centers of the co-linear apertures be s_{sd}. The flux transferred between the two apertures is given by

$$\phi = \frac{2L(\pi r_s r_d)^2}{r_s^2 + r_d^2 + s_{sd}^2 + \left[\left(r_s^2 + r_d^2 + s_{sd}^2\right)^2 - 4r_s^2 r_d^2\right]^{1/2}}, \tag{3.7}$$

where L is the radiance of the source. For the typical experiment, where $\left(r_s^2 + r_d^2 + s_{sd}^2\right) \gg 2r_s r_d$, Eq. (3.7) can be reduced to

$$\phi = \frac{L(\pi r_s r_d)^2}{r_s^2 + r_d^2 + s_{sd}^2}. \tag{3.8}$$

From Eq. (3.8), the irradiance at a detector can be obtained as

$$E = \frac{\phi}{A_d} \cong \frac{LA_s}{r_s^2 + r_d^2 + s_{sd}^2}, \tag{3.9}$$

where A_s and A_d are the areas of the source aperture and detector aperture, respectively. The separation between the two defining apertures is often much greater than the radii of the apertures themselves. In this case, Eq. (3.9) can be reduced to the inverse squared law for a point-source,

$$E \cong \frac{LA_s}{s_{sd}^2}. \tag{3.10}$$

The separation between the source and detector apertures is determined radiometrically by measuring the signal as a function of position and using Eq. (3.9) or Eq. (3.10). The position of the detector (or source) is measured using a linear encoder (see Fig. 1).

B. Tunable laser developments

Lasers come in a myriad of forms, each having distinct temporal, spatial, and spectral characteristics. SIRCUS uses both pulsed laser systems and continuous-wave (cw) laser systems. The pulsed lasers range from quasi-cw, mode-locked femtosecond, and picosecond systems operating at repetition rates on the order of 80 MHz to 100 MHz to Q-switched systems operating at a repetition rate of 1 kHz. The laser gain medium can be either a liquid, e.g., flowing dye, or a solid element such as a crystal or an optical fiber. Historically, solid state Ti:sapphire lasers and dye lasers have been the workhorses of the SIRCUS tunable laser systems. They operate over the spectral range from 560 nm to 1150 nm. A commercial Optical Parametric Oscillator (OPO) extends the spectral range from 1150 nm to 2500 nm, while spectral coverage is extended into the ultraviolet by frequency doubling, tripling, and quadrupling the output from a commercial mode-locked Ti:sapphire laser. In the mid-wave infrared region, cw OPOs that cover the spectral range from 1.4 μm to 4.5 μm[20] are used on SIRCUS. Finally, while not currently installed in SIRCUS, Quantum Cascade Lasers (QCL's) are commercially available for the 3.5 μm to 11 μm spectral region.[21]

Lithium Tri-Borate (LBO) OPO's have been around since the mid 1990s;[22–26] commercial short pulse, mode-locked, and cw LBO OPO's covering the range from the UV into the mid-infrared spectral region have been developed.[27] Practical use of many of these systems is limited by the complexity of the system, lack of stability in the output power, and the inability to automatically tune the output wavelength of the system. These limitations require continuous laser monitoring and adjustment, greatly increasing the time and cost of a calibration. In Sec. III B 1, a custom NIST-developed, mode-locked picosecond (psec) LBO OPO system is described that has high output power, narrow linewidth, and fully automated tuning over the spectral range from 340 nm to 2300 nm. It is intended to be the new primary SIRCUS calibration laser source over this spectral range. In Sec. III B 2, the use of a Q-switched OPO system operating at 1 kHz is described. The kHz OPO systems are commercially available with computer controlled, user-selectable output wavelengths; they serve as an alternate calibration source to the LBO OPO system. In addition to uses for SIRCUS calibrations, the kHz OPO system and a supercontinuum-source pumped laser-line tunable filter system are being evaluated for potential use with cryogenic radiometers.

1. MHz LBO OPO system

The custom-built, synchronously pumped, mode-locked psec LBO OPO, quasi-cw system with an 80 MHz repetition rate is computer controlled over the full output range of the system. Temperature tuning of the LBO crystal allows parametric oscillation from 680 nm to 1150 nm in the primary optical cavity. Idler light from 1150 nm to 2300 nm is extracted through a cavity mirror. Our system consists of two LBO OPO cavities, a primary, conventional LBO OPO cavity and a second, intra-cavity doubled LBO OPO that produces light from 560 nm to 750 nm. A separate beam path through a Bismuth Borate (BiBO) crystal doubles the light from the primary optical cavity, resulting in a tuning range from 340 nm to 575 nm. Utilizing all 3 components, the wavelength range from 340 nm to 2300 nm can be accessed. The properties of the existing system are described below.

The main ring cavity, shown schematically in Fig. 8, is driven by a 20 W, 532 nm, 15 ps, 80 MHz laser.[28] Laser pulses are focused into a 30 mm long LBO crystal to a beam waist of about 40 μm. The astigmatically compensated[29] ring cavity is comprised of two 20 cm to 30 cm concave high-reflecting

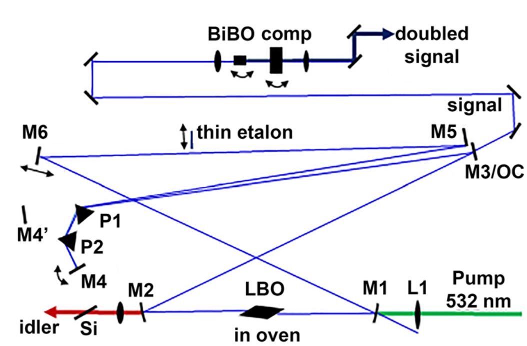

FIG. 8. Schematic diagram of the LBO OPO system with a BiBO doubler.

mirrors (M1 and M2) and 3 flat high reflectors (M4, M5, and M6). M3 is an 85% reflecting output coupler (the green pump laser beam travels with it for alignment—to remove the green beam, simply change the output coupler to the M6 position). Mirror M4′ is used when first assembling the OPO and aids tremendously in alignment. Two SF 10 Brewster prisms limit the linewidth to less than 1 nm. The prisms also allow tuning to within a few nm of the 1064 nm degeneracy. Idler lasing has been observed out to 1160 nm. The signal linewidth is typically 0.1 nm, and the idler wavelength is typically several times broader, Fig. 9. The temporal stability of the output wavelength is shown in Fig. 10, where the wavelength is stable to better than 0.001 nm over 1000 s. A thin etalon can be added for a narrower linewidth and a more stable wavelength.

The signal exits through mirror M3 and is either directed into the source or into the BiBO frequency doubler.[30] A compensating block is rotated to hold the doubled beam stationary, while the OPO is tuned. The compensating block is necessary to maintain efficient coupling into an optical fiber, for example, as the wavelength is tuned. The non-resonant idler exits the cavity through M2 and is collimated with a CaF_2 lens. Residual 532 nm pump light is removed with a Si filter. For signal wavelengths within the near-infrared (NIR) water absorption bands (≈920 nm to 1000 nm), we purge with dry N_2 to facilitate easier tuning and a more stable output.

To tune the OPO, the temperature of the LBO crystal is changed to allow for phase matching at the new wavelength,

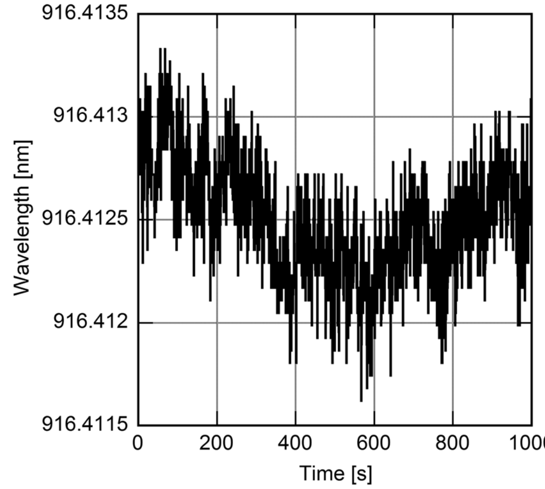

FIG. 10. Stability of the signal wavelength vs. time at 916.41 nm.

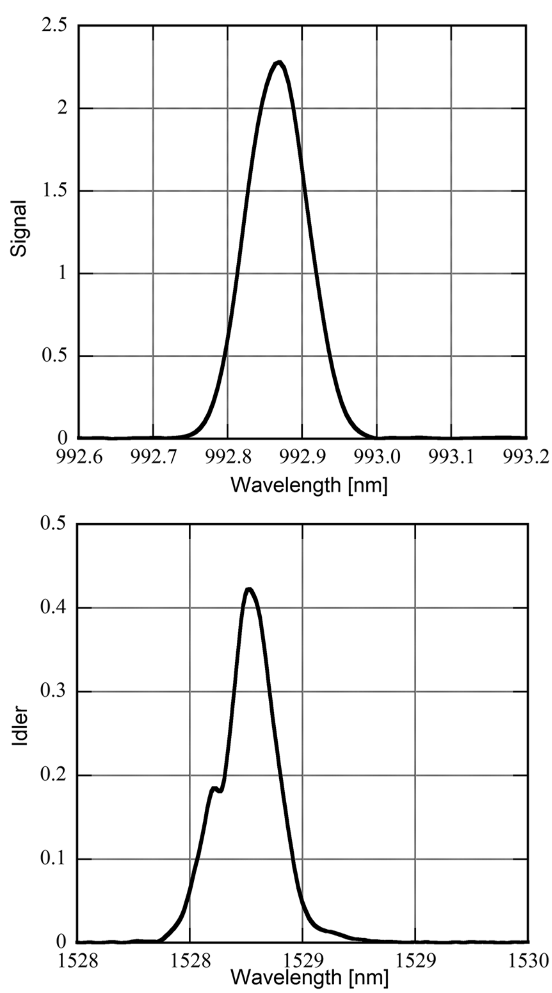

FIG. 9. Typical bandwidth of the signal (top) and the idler (bottom).

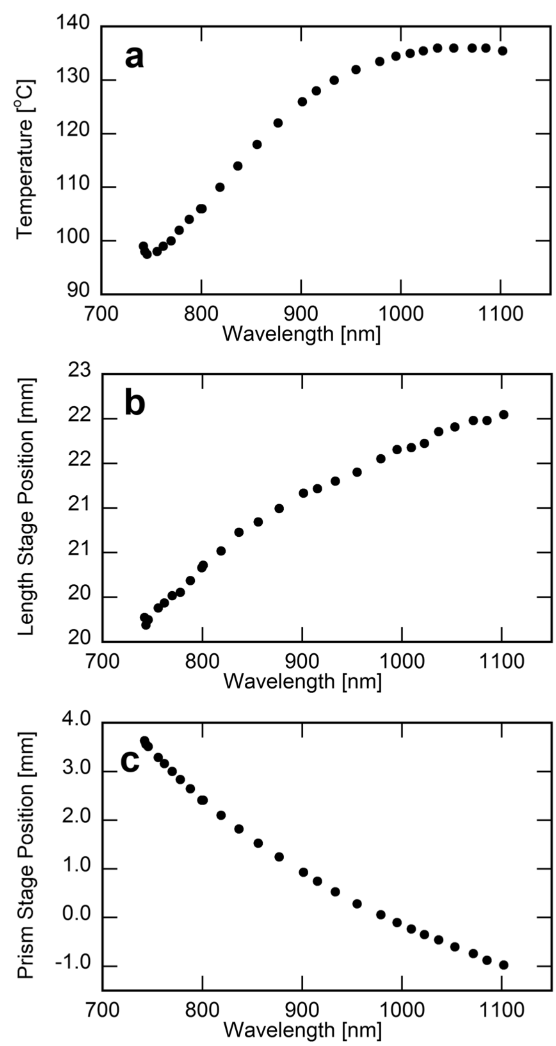

FIG. 11. Representative LBO OPO temperature (a), rotation (b), and distance (c) tuning curves.

mirror M4 is rotated, and M6 is translated to compensate for the dispersion in the LBO crystal and the change in the cavity length distance caused by the M4 rotation. The translation stages and LBO oven are computer controlled and a look-up table for the three parameters (temperature, rotation, and translation) enables the wavelength selection; Fig. 11 gives representative tuning curves.

Historically, Rhodamine 6G and DCM dye lasers covered the spectral region from 565 nm to 680 nm. To cover this spectral region with the custom OPO system, an intracavity doubled LBO OPO laser was developed. The optical layout is similar to the layout of the primary cavity shown in Fig. 8. However, in this case, a second beam waist is positioned within the cavity and a second LBO crystal is positioned there, as shown in Fig. 12. All mirrors except M8 are high reflectors from about 1000 nm to 1500 nm. Mirror M7 is highly transparent to the doubled light (560 nm to 750 nm). M8 is a 97.5% reflective output coupler in the present setup and allows for tunable light in the hundreds of mW range from 1000 nm to 1500 nm. This also allows a readily available beam to help align the primary OPO. The LBO doubling crystal is temperature tuned for non-critical phase matching (see Fig. 13), so no angular adjustments are required. For tuning, the OPO LBO temperature must be adjusted, the doubler LBO crystal temperature needs to be independently adjusted, mirror M4 needs to be adjusted in angle, and another cavity mirror needs to be translated. As with the primary OPO system, the adjustments are all automated and based on a lookup table.

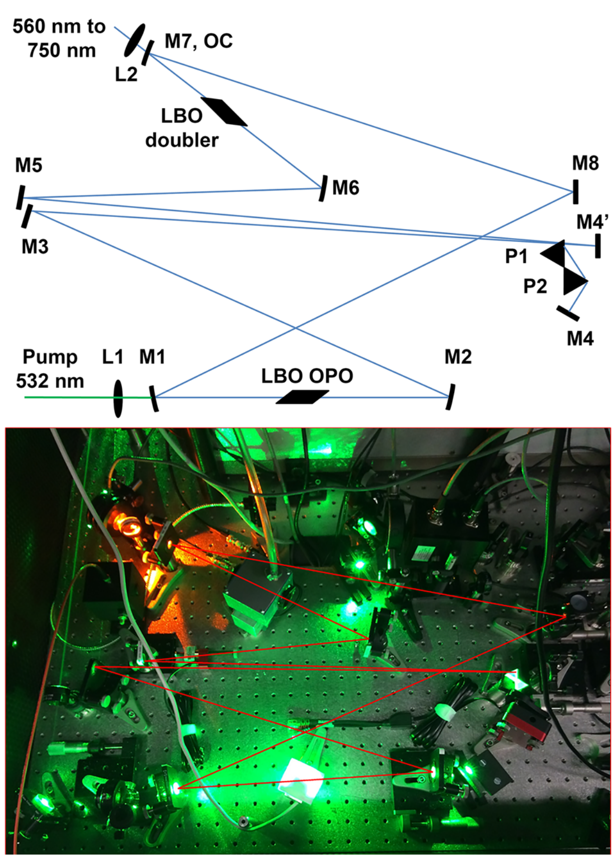

FIG. 12. Schematic diagram of the intracavity doubled OPO (top) and outlined photograph of the doubling cavity (bottom).

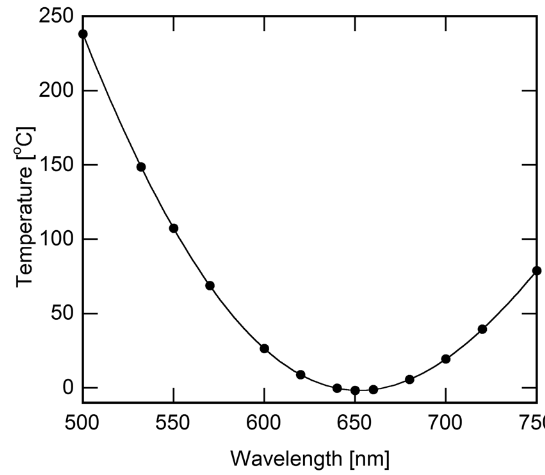

FIG. 13. Plot of the LBO OPO doubler crystal temperature vs. wavelength as calculated using the SNLO software.

With the two OPO cavities, we are able to produce output powers of hundreds of mW from 340 nm to 2300 nm with output powers greater than 1 W over much of the range, Fig. 14. Work continues to extend the spectral coverage of the system into the UV by mixing the signal output with the pump laser (at 532 nm). An alternative approach to cover the UV involves frequency doubling the output of the intracavity-doubled OPO in a beta-Barium Borate (BBO) crystal.

2. kHz LBO OPO system

Recently developed, commercially available Q-switched OPO-based tunable lasers with kHz repetition rates and nanosecond (ns) pulse lengths[31] offer a different approach to detector calibrations. These systems are more affordable than alternative approaches such as a series of tunable CW lasers pumped by a mainframe argon ion laser or a pulsed mode-locked system with a Ti:sapphire laser. The kHz OPO systems

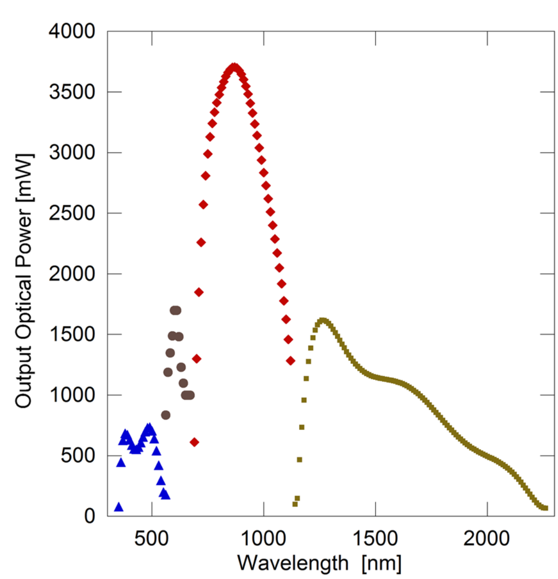

FIG. 14. LBO OPO output power as a function of wavelength. Red diamonds for the signal, orange squares for the idler, blue triangles for the BiBO doubled signal, and brown circles for the intracavity doubled LBO.

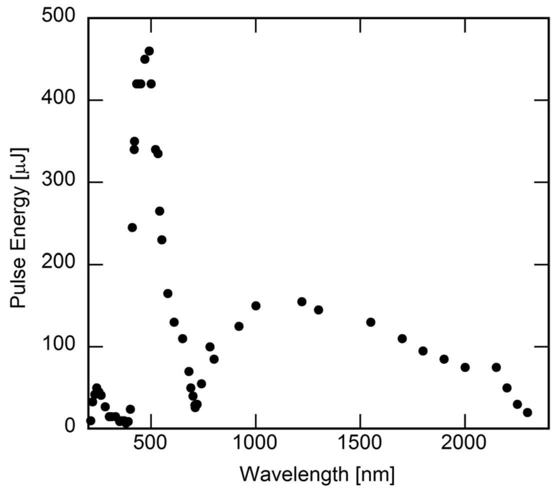

FIG. 15. Output pulse energy of an Ekspla Q-switched OPO system.

are fully automated over a spectral range from 210 nm to 2500 nm with laser power on the order of 100 mW in the visible range, Fig. 15. The spectral widths of the laser at wavelengths of 350 nm, 600 nm, and 1100 nm, shown in Fig. 16, are 0.08 nm, 0.14 nm, and 0.48 nm, respectively, which correspond to linewidths of 6.5 cm^{-1}, 3.89 cm^{-1}, and 3.96 cm^{-1}. The finite spectral width serves to reduce the magnitude of interference fringes originating from optical elements of detectors (e.g., windows) and instruments (e.g., filters). Unlike picosecond or femtosecond laser pulses, nanosecond laser pulses can be difficult to temporally stretch. Figure 17 shows the measured pulse width of the output from the OPO laser after the OPO laser beam propagates through a 5 m length of multimode optical fiber and after the laser beam is introduced into a 50 mm diameter integrating sphere. The measured width of the OPO laser pulse after propagating through the 5 m multimode optical fiber is essentially the same as the original pulse width. Therefore, an optical fiber is not useful to stretch the pulsed width of a ns OPO laser, unlike fs or ps pulsed lasers. The laser pulse is only slightly stretched—from 4 ns to 6 ns, when measured at the exit port of the 50 mm integrating sphere using a high-speed detector and a high-speed oscilloscope. The 2 ns stretch of the pulse width is due to the multiple reflections of the laser beam inside the 50 mm integrating sphere with 98% coating reflectance.

With pulse widths on the order of a few ns, the duty cycle of a kHz OPO laser is approximately 10^{-5}. This low duty cycle causes saturation problems when conventional measurement systems, consisting of a detector, a trans-impedance amplifier, and a digital multimeter, are used. A voltage or current

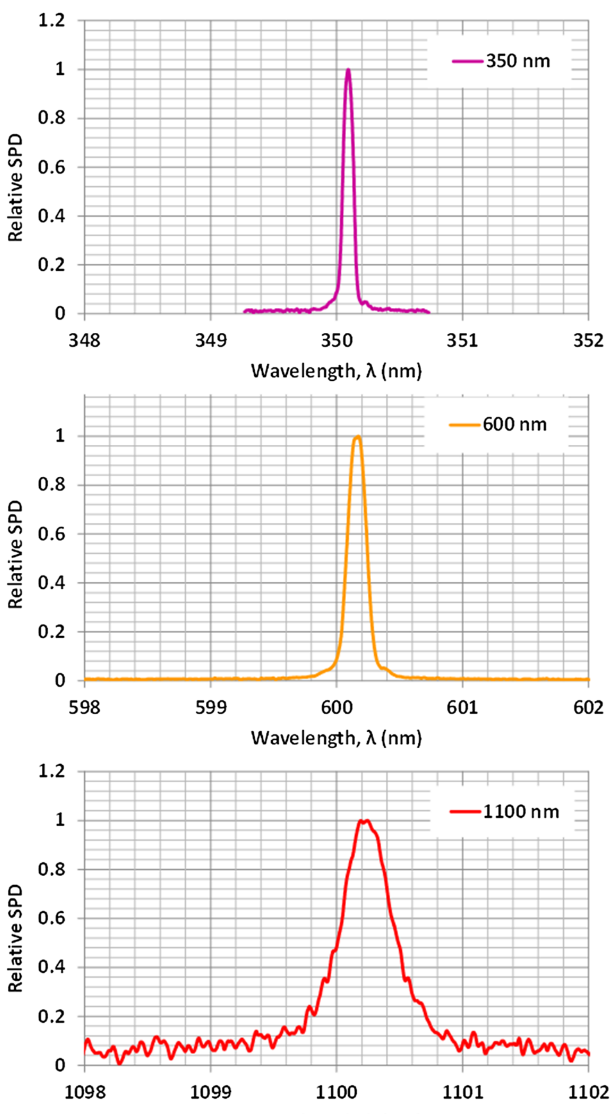

FIG. 16. Spectral widths of the output of the kHz OPO system at 350 nm, 600 nm, and 1100 nm.

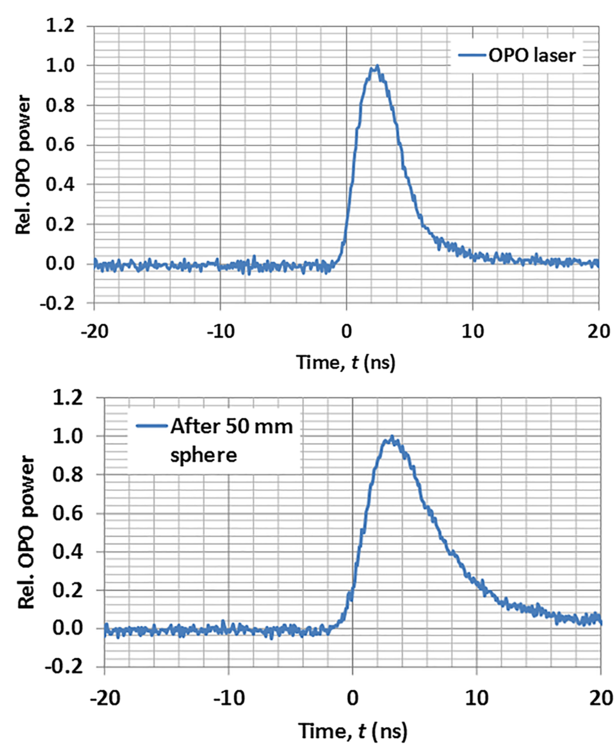

FIG. 17. Oscilloscope traces of the LBO OPO relative output power before (top) and after (bottom) propagation through the 50 mm SIS. Reprinted with permission from Zong *et al.*, Metrologia **49**, S124-S129 (2012). Copyright 2012 IOP Publishing.

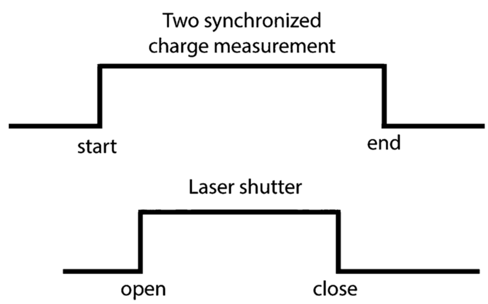

FIG. 18. Time sequence of the measurement of a pulsed laser train. Reprinted with permission from Zong *et al.*, Metrologia **49**, S124-S129 (2012). Copyright 2012 IOP Publishing.

integrator is used with these systems to reduce effects of saturation while accounting for laser pulse-to-pulse fluctuations, which can be on the order of 10%. Both approaches (voltage or current integration) can reduce the overall uncertainty in the source radiant flux to 0.1% or lower.

The current integration approach is based on the measurement of the total energy of a pulsed laser train using two synchronized current integrators (also called charge amplifiers) to measure the total electric charge from a test detector and a reference standard detector, respectively.[32] The substitution method is typically used and a monitor detector accounts for differences in the laser intensity between measurements by the test detector and the reference standard detector. Measurements between the test detector (or the reference standard detector) and the monitor detector are synchronized. Figure 18 shows the time sequence for the measurement of a pulsed laser train. The interval between the measurement start time and the laser shutter opening and that from the laser shutter closing and the measurement end time should be kept short to minimize the dark signal (e.g., 1 s). However, the timing is not critical if dark subtraction is applied or the measured dark signal is negligible. The test detector and the standard trap detector are aligned, in turn, to measure a pulsed laser train over a period of time. The entire measurement sequence is controlled by a computer.

A schematic diagram of the measurement setup is shown in Fig. 19. Two electrometers measure the total electric charge from the monitor detector and either the reference standard

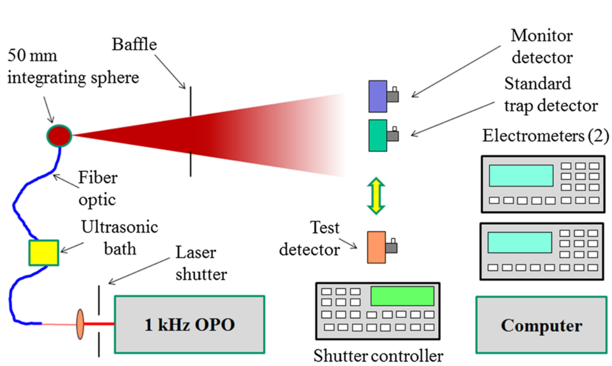

FIG. 19. Schematic diagram of the kHz laser-based calibration system. Reprinted with permission from Zong *et al.*, Metrologia **49**, S124-S129 (2012). Copyright 2012 IOP Publishing.

detector or the test detector. The total charge, Q, of a pulse train, $i(t)$, of photocurrent of a detector is obtained by

$$Q = \int_0^T i(t)dt = C \times V, \tag{3.11}$$

where T is the length of a pulse train (unit: s), C is the capacitance of the feedback capacitor of the operational charge amplifier, and V is the output voltage of the operational charge amplifier. The electrometer bias current and burden voltage are 3 fA and 20 μV, respectively. A plug-in 10-channel multiplexer is used for charge measurements for the test detector and the standard trap detector so that the meter-to-meter systematic error is eliminated in the calibration.

The non-linear response of a photodiode type must be investigated when a pulsed laser is used as a calibration source due to concerns about saturation at pulse peak intensity levels. As an example, a silicon photodiode (Hamamatsu, Model S2281) was tested for non-linearity using the kHz OPO at 450 nm with the same setup, as shown in Fig. 19.[32] A silicon photodiode, identical to the test photodiode, was used as the reference detector for this test. The light level of the reference detector was reduced two orders of magnitude lower than that of the test photodiode, and, thus, its non-linearity was negligible compared with that of the test detector. Test results showed that the non-linearity threshold value of this particular test photodiode is at an averaged photocurrent of approximately 1×10^{-6} A (corresponding to a peak photocurrent of 1×10^{-1} A or 100 mA), which is 2 to 3 orders of magnitude lower than a typical non-linear threshold value for the measurement of a dc light source. On the other hand, the peak threshold photocurrent is 2 to 3 orders of magnitude higher than a typical dc threshold value. Note that the non-linearity threshold value depends not only on the detector but also on the wavelength, pulse width, repetition rate, and duty cycle of the pulsed source.

The spectral irradiance responsivity of the test detector, $R_{\text{test}}(\lambda)$, is given by

$$R_{\text{test}}(\lambda) = \frac{(Q^{\text{s}}_{\text{test}} - Q^{\text{d}}_{\text{test}})}{\left(Q^{\text{s, test}}_{\text{monitor}} - Q^{\text{d, test}}_{\text{monitor}}\right)} \Bigg/ \frac{(Q^{\text{s}}_{\text{standard}} - Q^{\text{d}}_{\text{standard}})}{\left(Q^{\text{s, standard}}_{\text{monitor}} - Q^{\text{d, standard}}_{\text{monitor}}\right)} \times R_{\text{standard}}(\lambda), \tag{3.12}$$

where $Q^{\text{s}}_{\text{test}}$ and $Q^{\text{d}}_{\text{test}}$ are the total charges accumulated by the test detector for laser and dark measurements, respectively; $Q^{\text{s, test}}_{\text{monitor}}$ and $Q^{\text{d, test}}_{\text{monitor}}$ are the total accumulated charges of the monitor detector when the test detector is used. Correspondingly, $Q^{\text{s}}_{\text{standard}}$ and $Q^{\text{d}}_{\text{standard}}$ are the total charges of the standard trap detector for laser and dark measurements, respectively; $Q^{\text{s, standard}}_{\text{monitor}}$ and $Q^{\text{d, standard}}_{\text{monitor}}$ are the total charges of the monitor detector when the standard trap detector is used. $R_{\text{standard}}(\lambda)$ is the spectral irradiance responsivity of the standard trap detector.

A test silicon photodiode (Hamamatsu Model S2281) was calibrated against a standard trap detector for spectral irradiance responsivities using the kHz OPO. To establish the measurement uncertainty, the calibration system was first tested for measurement repeatability, which is on the order of 10 ppm for both detectors.[32] The integration time (pulse train length) for each measurement is approximately 1 s, which corresponds to ≈1000 pulses.

The test detector was calibrated at several wavelengths for absolute spectral irradiance responsivity. In addition to the pulsed 1 kHz OPO laser, a CW argon-ion laser and four CW helium-neon lasers with laser line filters were used to validate the new calibration method. The OPO pulsed laser was tuned to be at the same wavelengths as that of CW lasers for this calibration. The test detector was first calibrated by using the 1 kHz pulsed laser with the two electrometers with a charge amplifier for the measurement of total charge of the test detector and monitor detector at seven wavelengths of 458 nm, 488 nm, 514 nm, 543.5 nm, 594 nm, 612 nm, and 632.8 nm. Then the 1 kHz pulsed laser was replaced by the CW lasers for calibration at four wavelengths of 458 nm, 488 nm, 514 nm, and 632.8 nm. Finally, the two electrometers were replaced by two trans-impedance amplifiers for calibration of the test detector at all seven wavelengths of 458 nm, 488 nm, 514 nm, 543.5 nm, 594 nm, 612 nm, and 632.8 nm under DC mode using the conventional trans-impedance amplifier scheme. The CW lasers were stabilized by using a laser power controller (LPC) for the calibration under DC mode.

The three different calibration methods were compared and the relative differences at the measured wavelengths are shown in Fig. 20. The difference in calibration results between the electrometers and the trans-impedance amplifiers using CW lasers is given by blue diamonds. The average difference is approximately 0.02%, an indication that charge amplifiers are equivalent to trans-impedance amplifiers for the measurement of CW sources. The red circles give the relative difference in responsivity obtained using the new calibration method (with a 1 kHz pulsed laser and charge amplifiers) and using the conventional calibration method (with a CW laser and two trans-impedance amplifiers). The average difference is also 0.02%. The comparison results show that there was a systematic difference of 0.02% between the charge amplifier-based system and the trans-impedance amplifier-based system, most likely due to the accuracy of amplifier's gain, and the change from the CW lasers to the tunable pulsed laser did not make a meaningful difference in the calibration results. These measurements demonstrate the equivalence between the kHz pulsed laser-based method and the CW laser-based method.

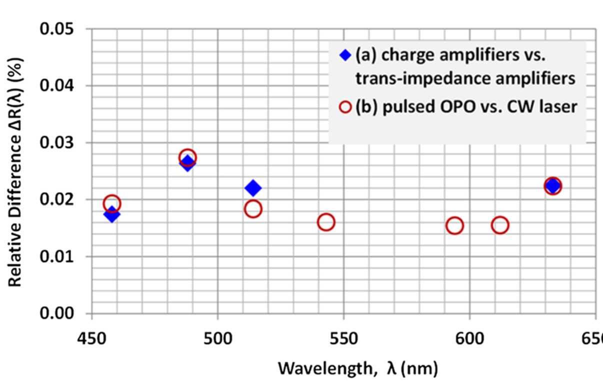

FIG. 20. Relative difference in measured responsivity between the electrometers and the trans-impedance amplifiers (blue diamonds) and between the kHz OPO-based calibration and the conventional calibration using cw lasers (red circles). Reprinted with permission from Zong *et al.*, Metrologia **49**, S124-S129 (2012). Copyright 2012 IOP Publishing.

TABLE I. Spectral irradiance responsivity calibration uncertainty budget using the kHz pulsed OPO system.

	Relative standard uncertainty (%)	
	Type A	Type B
Reference trap detector		0.019
Laser wavelength (0.02 nm)		0.005
Sphere source irradiance non-uniformity		0.005
Detector reference plane		0.010
Detector nonlinearity		0.005
Transfer to test detector	0.005	
Electrometer (relative only)		0.005
Combined uncertainty (%)	0.025	
Expanded uncertainty (k = 2) (%)	0.05	

An example spectral irradiance responsivity uncertainty budget using a 1 kHz pulsed OPO laser is shown in Table I. The expanded uncertainty with a coverage factor of k = 2 is 0.05%; the dominant component is the irradiance responsivity uncertainty of the standard trap detector. This method can be used in other applications, for example, in measurements of material properties of transmittance and reflectance.

C. Effect of laser power control

A laser intensity stabilizer, often referred to as a laser power controller (LPC), is used to stabilize the output of the laser. Figure 21 shows the effect of the LPC on the variance in a measurement. Three configurations are shown: no stabilizer, stabilizing using the internal detector with the LPC, and stabilizing on an external monitor detector mounted on the side wall of the ISS. For each configuration, approximately 48 s of data are acquired and the standard deviation is calculated. As shown in the figure, with no stabilization, the output from the ISS has a standard deviation of 2.1%. Stabilizing on the monitor internal to the LPC, the standard deviation in the output of the sphere is reduced an order of magnitude, to 0.26%. Finally, stabilizing the laser beam externally using a monitor photodiode mounted on the wall of the ISS reduces the measurement uncertainty an additional factor of 5, to 0.05%.

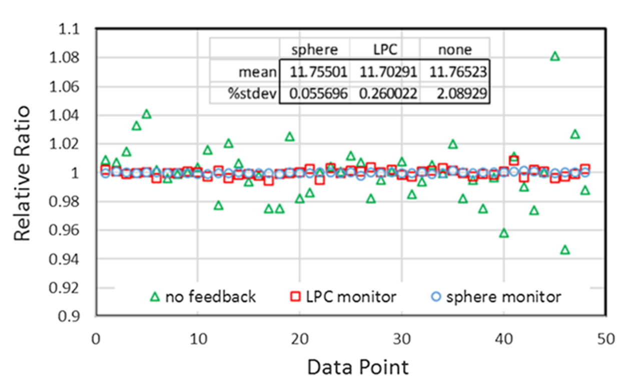

FIG. 21. Effect of laser power control on measurement fluctuations.

D. Effect of speckle on measurement uncertainty

Laser speckle is an interference on the detector between two different parts of a spatially coherent beam that travel slightly different distances as the beam is reflected off a target with different depths, like the surface wall of an integrating sphere source. Speckle increases the non-uniformity of the flux distribution at the detector and, because the interference pattern is dynamically changing, the variance in a measurement is affected as well. The variance in a measurement introduced by laser speckle can be reduced by shifting the dynamic speckle pattern to frequencies greater than the time constant of a measurement. Various approaches have been used to reduce measurement noise arising from laser speckle. For free-space laser propagation, techniques include the introduction of a moving diffuser in the laser beam path and raster scanning the beam inside the sphere with a galvanometer-driven mirror.[33] In the case of laser beam delivery using a multi-mode optical fiber, effects of speckle can be reduced by placing a short length of fiber in an ultrasonic bath,[34,35] with the dominant ultrasonic bath frequency ranging from 20 kHz to 40 kHz, as well as by using piezoelectric-based spatial mode scrambling and fiber stretching and rotating approaches.[36,37] Note that the speckle is still present, but the low frequency components are eliminated so that the speckle has a much shorter time constant than the observing radiometers, effectively averaging out the interference effects.

The NIST SIRCUS facility uses multimode optical fibers to deliver the laser radiation to the source and an ultrasonic bath to mix the spatial modes in the fiber. Typically, 1–2 m of the unjacketed fiber is submerged in the ultrasonic bath. Over time, small cracks are introduced into the fiber from the ultrasonic bath, reducing the transmittance of the fiber. This requires maintenance of the optical fiber, occasionally cutting off the part of the fiber that had been in the ultrasonic bath and preparing the next length of fiber to be put into the bath. We often use separate patch cables for the ultrasonic bath and simply replace them once the loss becomes excessive.

Figure 22 illustrates the effect of speckle on the measurement uncertainty. With the ultrasonic bath (speckle reducer) turned off, the measurement standard deviation is 29%; with the ultrasonic bath turned on, the standard deviation is 0.8%, a 35-fold reduction in the standard deviation of the measurement.

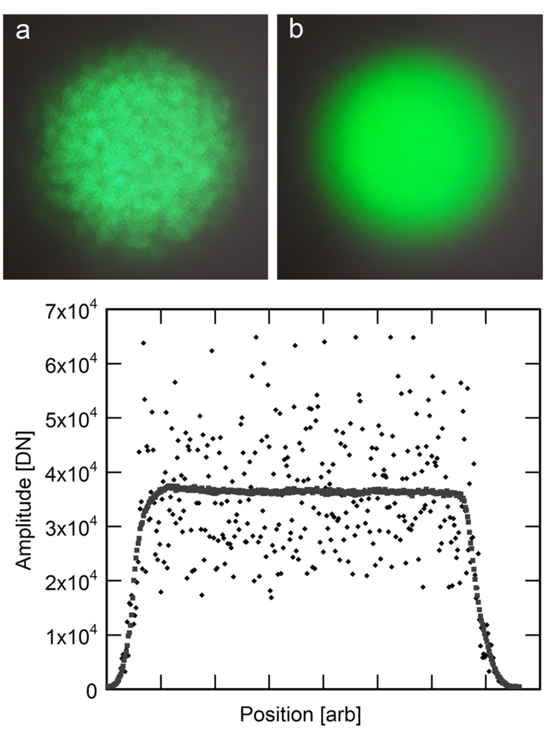

FIG. 22. (a) Output from a multimode optical fiber excited with 532 nm radiation (left). Output from the same fiber with the "speckle-eater" turned on (right). (b) Effect of laser speckle on the measurement uncertainty, showing the difference in measurement noise when the speckle eater (an ultrasonic bath) is turned on and off.

E. Interference fringes in an instrument's spectral responsivity

Frequently, interference features are seen in an instrument's spectral responsivity when continuous-wave (cw) lasers are used in the calibration due to their narrow bandwidths and high degree of temporal coherence. Commonly, interference fringes are observed in windowed detectors from reflections off the front and back surface of the window with amplitudes on the order of 0.5% to 1%, off the front and back surfaces of the Si detector, and in filter radiometers with multi-layer dielectric filters. Fringe amplitudes can be 15% and greater in multi-layer dielectric filters. To avoid interference fringes in the monitor signal caused by residual coherence in the output radiation of a sphere source, the window of the detector is removed or a diffuser is placed between the detector and the integrating sphere. For the DUT, interference fringes are effectively averaged out by increasing the bandwidth of the laser source, for example, by using ps or fs pulses.[38] Note however that the fringes do exist in the instrument's responsivity. Measuring sources with finite bandpass, the high frequency responsivity from fringes effectively averages out and the fringes do not impact the measurement.

A filter radiometer calibrated on SIRCUS using cw lasers with interference fringes with a peak-to-valley amplitude of

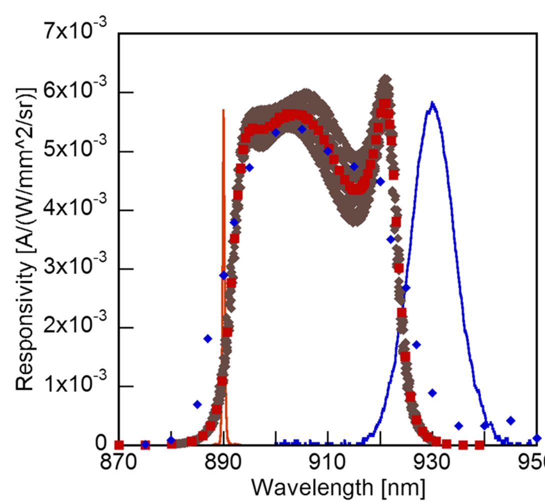

FIG. 23. Absolute spectral responsivity of a filter radiometer measured using cw, picosecond, and femtosecond lasers. Representative picosecond and femtosecond spectra are shown as well.

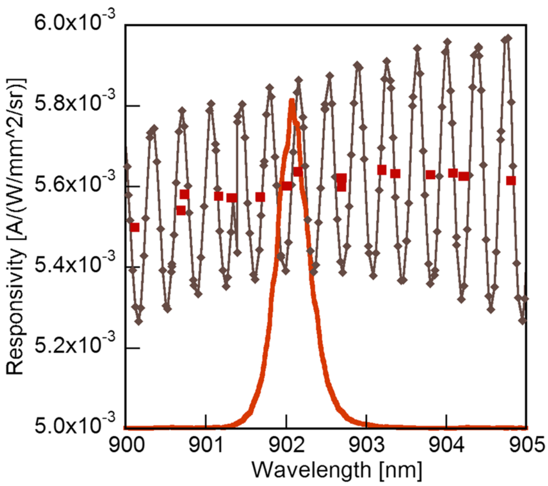

FIG. 24. Expansion of Fig. 23 around 902 nm illustrating the difference in the measured responsivity using cw, picosecond, and femtosecond lasers, respectively.

7% at 900 nm is shown in Fig. 23; the calibration was repeated using picosecond and femtosecond laser systems. The spectral widths of the ps and fs laser pulses are shown in the figure as well. Clearly, the bandwidth of the fs laser is too broad to accurately calibrate the filter radiometer. The ps laser, on the other hand, with a bandwidth of 1 nm, greatly reduced the magnitude of the interference effects, providing an accurate mean responsivity. Figure 24 is an expansion of Fig. 23 around 902 nm illustrating the impact of the use of the ps laser system on the measured responsivity. Band-integrated responsivities are the same using either the ps or the cw laser system.

F. Uncertainty budget

NIST SIRCUS calibrations of customer Device Under Test (DUT) are made by comparison to transfer standards that are traceable to the SI. The SI traceable calibration of the transfer standard along with the development of an uncertainty budget establishes SI traceability in the responsivity of the DUT.[1,39] Characterization elements of importance to the responsivity uncertainty budget include uniformity, linearity, temperature dependence, and temporal dependence. Details of the development of an uncertainty budget for silicon trap detectors are given in Ref. 1; principal components for trap detectors calibrated against POWR at three wavelengths[40] are listed in Table II. Table III lists the principal uncertainty components in the transfer of the radiometric scale from the transfer standard to a DUT.

TABLE II. Example summary results of the components of corrections and uncertainties for the measurement of the power responsivity of a trap detector using POWR at three laser wavelengths. The u value is the uncertainty associated with each component at $k = 1$. The u_{rel} is the same as u but expressed in terms of %.

	Wavelength (nm)		
	488	514.5	632.82
Optical power uncertainty	0.012 7	0.012 7	0.012 1
Type B uncertainties/corrections			
Trap spatial uniformity (U_s)	1	1	1
$u(U_s)$	9.71×10^{-5}	9.71×10^{-5}	9.26×10^{-5}
$u_{rel}(U_s)$	0.009 7	0.009 7	0.009 3
Trap amplifier gain (G)	1×10^4	1×10^4	1×10^4
$u_{rel}(G)$	0.004	0.004	0.004
Type A uncertainty in %	0.01	0.01	0.01
Trap responsivity in A/W (R_t)	0.391 680	0.413 307	0.509 205
Trap quantum efficiency	0.994 837	0.995 697	0.997 363
Combined uncertainty $u_{rel}(R_t)$ in %	0.019	0.019	0.019

TABLE III. Uncertainty budget for a transfer of the irradiance scale from NIST reference trap detectors to a device under test.

	Relative standard uncertainty (%)		
Uncertainty component	Type A		Type B
Reference detector responsivity			
Radiant power responsivity (400 nm to 920 nm)	0.019		
Aperture area	0.004		
Response uniformity	0.005		
Cosine dependence	0.010		
Polarization			0.000
Linearity	0.000		
Temperature			0.003
Source characteristics			
Radiant flux	0.005		
Wavelength (<0.01 nm)			0.005
Irradiance uniformity	0.005		
Determination of the reference plane			0.010
I-V gain	0.010		
Voltmeter reading			0.005
Irradiance		0.029	
Transfer to device under test (estimated)		0.030	
Combined standard uncertainty ($k = 1$) (%)		0.044	

Reference standard detectors are calibrated at regular intervals against ACRs to update their calibrations to account for any long-term variation that might occur with these detectors. Several reference trap detectors at SIRCUS have been

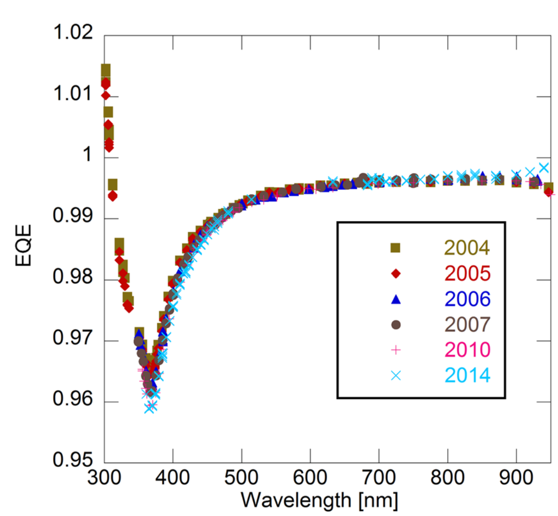

FIG. 25. Measurements of the EQE of a Si tunnel trap detector over 10 years.

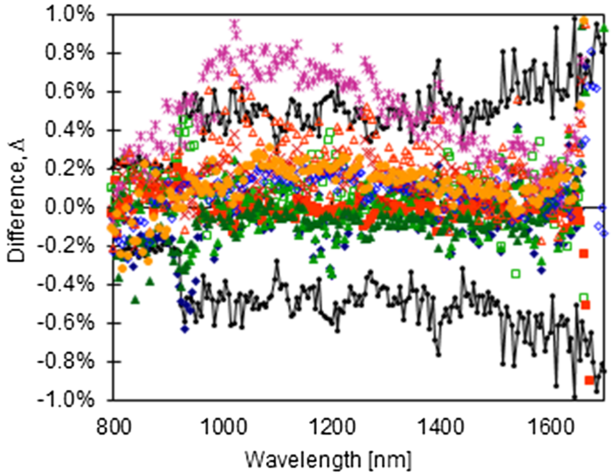

FIG. 26. Stability of InGaAs detectors over 6 years, measured on NIST's Spectral Comparator Facility. Colored symbols represent the difference from the initial mean. The measurement uncertainties (k = 1) are shown in black with the connecting line.

calibrated for many years. Shown in Fig. 25 is the EQE of a tunnel trap detector monitored over 10 years. Not all trap detectors exhibit this level of temporal stability: In general, transmittance trap detectors exhibit excellent stability in the visible and near-infrared ranges but tend to show a decrease in EQEs below 500 nm. Geist *et al.* attributed the reduction in EQEs to trapped charge at the Si–SiO_2 anti-reflection coating interface.[41,42] Exposure to UV light reduces the EQEs as well.[13] Figure 26 shows the typical stability of InGaAs photodiodes. As shown in the figure, the responsivity of the detector has not changed over 6 years, within the k = 1 measurement uncertainty.

The InGaAs uniformity is dominated by the internal structure of the photodiode and thus configuring the detectors in a trap design does not significantly improve the uniformity as it does for silicon where the reflectance dominates. For single element InGaAs detectors, the uncertainty in their power responsivity calibrated by POWR is dominated by the uniformity of the photodiode. A variation in the response of 0.2% or more is typical when raster scanning the laser beam across a photodiode. The uniformity of an example InGaAs photodiode is shown in Fig. 27. The uncertainty in irradiance calibrations using these InGaAs transfer standards increases to 0.4%. The integrating sphere/ext-InGaAs transfer standards have an uncertainty of 1% to 2%, principally due to the low throughput of the integrating sphere and its temporal stability.

Calibration of filter radiometers is a common SIRCUS application; filter radiometers are used in photometry, colorimetry, and radiance temperature, to name a few examples. Propagation of the uncertainty through fitting spectral data and for transfer to working standards and customer artifacts is given in Ref. 43. Gardner also developed an uncertainty budget for interpolated spectral data using both Lagrangian and cubic spline interpolations.[44]

IV. APPLICATION TO PRIMARY RADIOMETRIC QUANTITIES AND UNITS

NIST has provided calibrations of customer devices for spectral power responsivity in the Spectral Comparator Facility (SCF)[45] for over 40 years using working standard detectors traceable to cryogenic radiometers. Historically, 6 fixed laser lines and several Ti:sapphire laser lines spanning the Si range were used to transfer the scale between the cryogenic radiometer and the transfer standards. Consequently, to realize a scale of absolute spectral response (ASR), a combination of measurements—against the High Accuracy Cryogenic Radiometer (HACR)[46]—and modeling—for interpolation between measured laser lines[47,48]—was used. Because of the long history using a model of a trap detector's IQE to interpolate between calibration wavelengths, a scale was transferred to the trap detectors using the POWR ACR at approximately 30 wavelengths between 400 nm and 900 nm using the broadly tunable SIRCUS lasers. The SIRCUS measurements are used to validate the Gentile model.[12] Results are presented in Sec. IV A.

In 2000 and 2001, four multi-channel filter radiometers were used to compare the detector-based scale from SIRCUS to the source-based radiance scale from NIST's Facility for Automated Spectroradiometric Calibrations (FASCAL)[49] using the NIST Portable Radiance (NPR) source[50] for the comparison.[51] The determination of the radiance of the NPR source is traceable to the freezing temperature of gold.

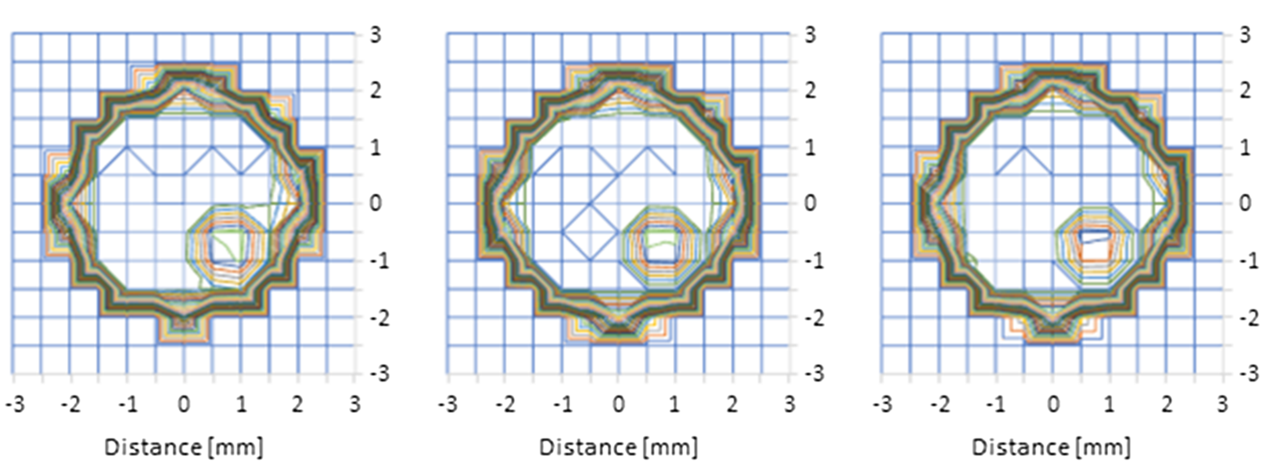

FIG. 27. Spatial uniformity of an InGaAs detector at (left) 900 nm, (middle) 1250 nm, and (right) 1600 nm. 0.2% contours are shown.

By calibrating filter radiometers for radiance responsivity on SIRCUS and comparing measured versus predicted signals when measuring the NPR source, the detector-based and source-based radiance scales can be compared. Results were in agreement within the combined expanded uncertainties, validating the uncertainty estimates of both the detector-based and the source-based methods. In Sec. IV B, extension of the comparison between a SIRCUS-based radiance responsivity of a filter radiometer—in this case a radiation thermometer—and the melting/freezing temperature(s) of a primary standard gold blackbody source is presented.

A. Validation of a trap detector quantum efficiency model

The SIRCUS facility has broadly tunable narrow-band lasers that cover the full spectral range of the model for the trap detector responsivity. Historically, eleven fixed laser lines were used in the derivation of trap detector power responsivity scales. This relatively sparse coverage over a 500 nm spectral window required a model to provide values at the other wavelengths. To validate the model used by the SCF to disseminate spectral power responsivity scales over the silicon range, Gentile *et al.*[12] compared the modeled IQE of silicon photodiodes as a function of wavelength to the measured IQE of 3 transmission trap detectors along with their transmittances at a large number of wavelengths. Figure 28 shows the difference between the modeled EQE of a tunnel trap detector (fit) and the measured EQE (data): The results of the test established that the model agreed with the measurements to within 0.01% over the full spectral range for all 3 trap detectors. The results imply that the model can be used to interpolate between a fairly small number of measurements with an accuracy comparable to the measurement accuracy. It is particularly useful for interpolation to a particular wavelength not exactly at one of the laser lines used for calibration.

B. Development of a detector-based thermodynamic temperature scale

The NIST Sensor Science Division is responsible for maintaining two fundamental SI units, the unit for temperature, the kelvin, above the melting point of gold and the unit for luminous intensity, the candela. The upcoming redefinition of the SI[52] will result in units which are based upon constants of nature instead of physical artifacts. The unit of temperature, the kelvin, instead of being defined by the triple-point of water, will be based upon a fixed Boltzmann constant, and thermodynamic temperatures can be determined using equations which relate measurable quantities to temperature. There are numerous techniques to measure thermodynamic temperatures, among them constant-volume gas thermometry, acoustic-gas thermometry, dielectric-gas thermometry, Johnson-noise thermometry, and spectral-radiation and total-radiation thermometry. The thermal energy or the thermodynamic temperatures of objects can be directly determined in each of these methods by separate extrinsic measurements using equations which relate thermodynamic temperatures to other measurands. The Consultative Committee for Thermometry which gives advice on matters of temperature to the

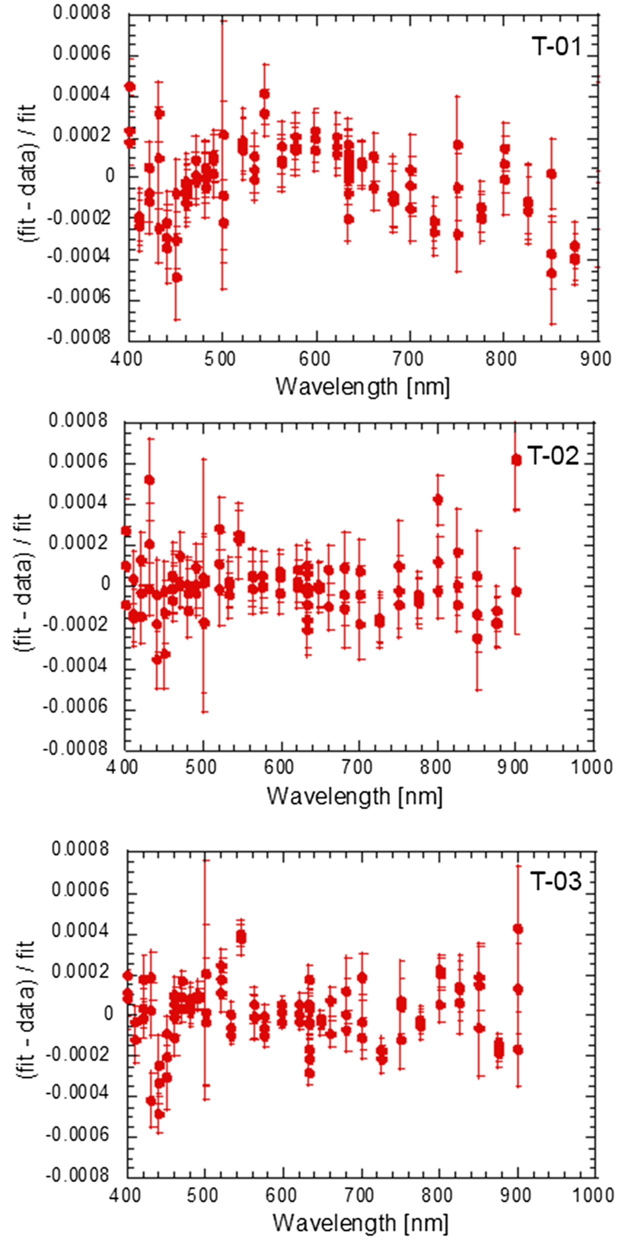

FIG. 28. Comparison between measured (symbol) and modeled (symbol) EQEs of a Si tunnel trap detector.

International Committee for Weights and Measures has recognized two of the above thermometric methods, acoustic-gas thermometry and spectral-radiation thermometry, as having sufficiently low uncertainties for inclusion in the *mise en pratique* for the realization of the kelvin.[53]

For temperatures above the freezing temperature of silver, the currently used International Temperature Scale of 1990 (ITS-90)[54] is defined in terms of spectral radiance ratios to one of the silver-, gold-, or copper-freezing temperature blackbodies using the Planck radiance law.[55] Because of the use of spectral radiance ratios, the temperature uncertainties of ITS-90 assigned blackbody, $u(T_{BB})$, increase as the square of the temperature ratios according to

$$u(T_{BB}) = \frac{u(T_{FP})}{T_{FP}^2} T_{BB}^2, \tag{4.1}$$

where T_{FP} and $u(T_{FP})$ are the temperature and the uncertainty of the fixed-point blackbody and T_{BB} is the temperature of the higher temperature blackbody. The thermodynamic temperature uncertainties are further increased because the assigned temperatures for the Al, Ag, and Au freezing-points in the ITS-90 result from thermometry using ratio pyrometry from the mean of two different and conflicting constant-volume gas thermometry measurements at lower temperatures.[56,57]

In the following, we describe the impact of tunable laser-based calibrations on reference standard radiation thermometers used to measure the thermodynamic temperatures of blackbody sources. In its simplest form, a radiation thermometer consists of input optics, a filter to select a spectral range of interest, and a detector.[58] Planck's law describes the spectral radiance emitted by a blackbody at temperature T,

$$L(\lambda, T)d\lambda = \varepsilon(\lambda) \cdot \left(2hc^2/n^2\lambda^5\right) \cdot \frac{d\lambda}{\exp(hc/n\lambda kT) - 1}, \quad (4.2)$$

where k is the Boltzmann constant, h is the Planck constant, c is the speed of light, n is the refractive index of the medium where the measurements are being performed, λ is the wavelength, and $\varepsilon(\lambda)$ is the spectral emissivity of the blackbody.[59]

The signal from the radiation thermometer is converted to a temperature using the measurement equation

$$i_u = \int s_L(\lambda)\, \varepsilon_u\, L_u(\lambda, T)\, d\lambda, \quad (4.3)$$

where $s_L(\lambda)$ is the absolute spectral responsivity of the radiation thermometer, ε_u is the emissivity of the blackbody, and $L_u(\lambda,T)$ is the radiance of the blackbody derived from Planck's equation. Using radiation thermometers traceable to cryogenic radiometers to measure the radiance temperature of high temperature blackbodies can result in uncertainties in measurements of temperature lower than those measured using the ITS-90 techniques.[59,60]

The calibration of the NIST Absolute Pyrometer 1 (AP1) is an example of the NIST SIRCUS calibrations applied to thermodynamic temperature measurements.[56,61] The AP1 was calibrated for absolute spectral radiance responsivity on SIRCUS; its spectral radiance responsivity is shown in Fig. 29 along with the spectral radiance distribution of a gold melting point blackbody at the ITS-90 temperature of 1337.33 K. The AP1 has a peak responsivity between 647 nm and 652 nm, a full-width half-maximum (FWHM) bandwidth of approximately 10 nm, and out-of-band blocking better than 10^{-7}. Interference fringes with an amplitude of 0.5% were observed in the responsivity; these fringes are not problematic if they are measured with sufficient wavelength accuracy. The in-band (IB) absolute spectral responsivity was therefore measured with 0.03 nm resolution to map out the interference fringes. Figure 30 shows an expanded view of the interference fringes seen in four determinations of the spectral responsivity of the AP1. The interference fringes in the spectral responsivities overlap very well, with the magnitude of the calibration in June 2003 being a few tenths of a percent higher than subsequent calibrations.

The AP1 measured the melt and freeze cycles of silver and gold fixed-point blackbodies. Figure 31 shows repeat calibrations over 3 days in May 2003. The noise-equivalent temperature at the gold (and silver) freezing temperature is ≈2 mK, and the noise will not be the dominant component of the total temperature uncertainties. Using the 2003 SIRCUS calibration of the AP1, the expanded uncertainty (k = 2) in the radiometric measurement of the gold (or silver) freezing-point blackbody was approximately 0.15%. The radiometric

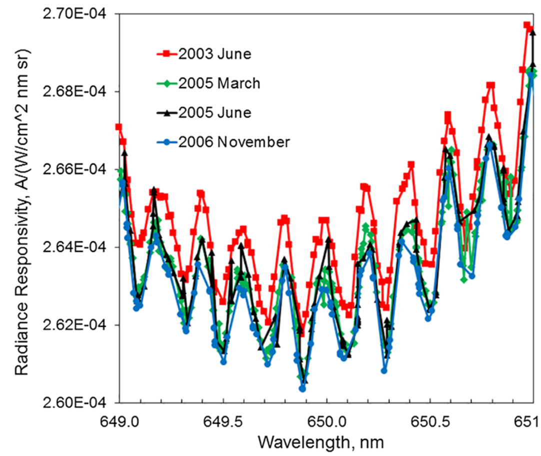

FIG. 30. Expanded view of the interference fringes seen in four determinations of the spectral responsivity of the AP1.

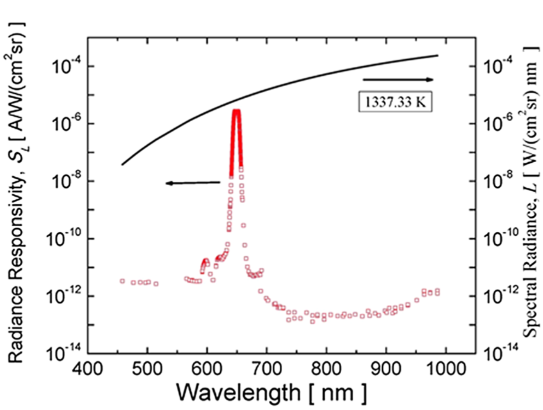

FIG. 29. ASR of the AP-1 and the spectral radiance of a primary standard gold melting point blackbody (at 1337.33 K).

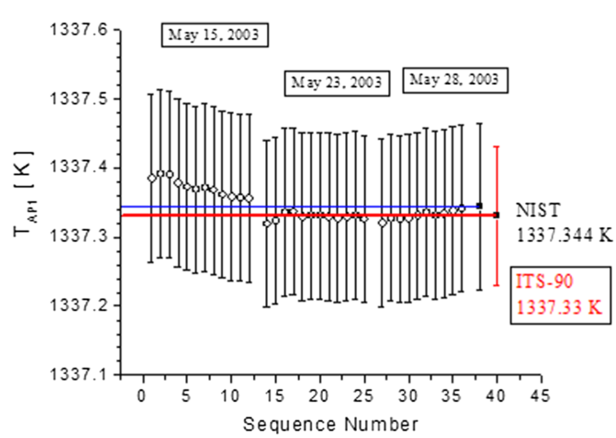

FIG. 31. Repeat measurements of a gold-point blackbody by the AP-1. The mean temperature determined by the AP-1 measurements is compared with the ITS-90 temperature.

TABLE IV. Gold and silver melting-point blackbody temperature based on the Advanced Pyromenter-1 (AP-1) calibrated on SIRCUS, the expanded (k = 2) measurement uncertainty in temperature, ITS-90 determination of the melting points of the gold and silver blackbodies, the expanded uncertainty in the ITS-90 determination of temperature, and the differences in the AP-1-based and ITS-90 based determinations of blackbody temperatures.

	T_{AP1} (K)	u (T_{AP1}) (K) (k = 2)	T_{90} (K)	u (T_{90}) (K) (k = 2)	T_{AP1}-T_{90} (K)
Au-point blackbody	1337.344	0.121	1337.33	0.100	0.014
Ag-point blackbody	1234.956	0.106	1234.93	0.080	0.026

uncertainties can be related to the uncertainties of the temperature determinations from the derivative of the Wien approximation, which shows the relationship between the uncertainty in radiance, L, to the uncertainty in blackbody temperature, T,

$$\frac{\Delta L}{L} = \frac{c_2}{\lambda}\frac{\Delta T}{T^2}. \tag{4.4}$$

In Eq. (4.4), c_2 is the second radiation constant, and λ is the wavelength. Using Eq. (4.4), an uncertainty of 0.15% in radiance responsivity at 650 nm will lead to an uncertainty of 121 mK in the measurement of the melting and freezing temperature of the gold-point blackbody, which is slightly larger than the ITS-90 uncertainty, as shown in Table IV.[56] The AP-1 was re-calibrated on SIRCUS using the 2004 detector responsivity scale. Using the new calibration, the expanded uncertainty in the radiometric measurement of the gold-point is reduced to approximately 0.09%. With the reduced uncertainty from SIRCUS, the corresponding temperature uncertainty derived from the uncertainty in the radiometric measurement of the gold-point blackbody can be reduced to approximately 72 mK, significantly lower than the 100 mK uncertainty in the ITS-90.[62]

Additional APs have been developed by NIST with changes to the design to further lower the uncertainties in the detector-based transfers. The use of radiation thermometers with filters and detectors sensitive to near-infrared radiation allows thermodynamic temperature measurements at temperatures as low as 400 K. The approach has been widely accepted by other NMIs who have developed or are developing detector-based radiation thermometer calibration facilities.[53,63]

V. EXAMPLE APPLICATIONS

The unique characteristics of tunable laser systems provide the versatility to address a wide range of optical metrology issues in addition to applications such as the realization of SI units or the calibration of customer detectors. The three applications presented below, the characterization of spectrographs for scattered light, the absolute calibration of the Suomi National Polar-orbiting Partnership (SNPP) Visible Infrared Radiometer Suite (VIIRS), and the characterization of the Kepler Camera (KeplerCam) at the Fred Lawrence Whipple Observatory in southern Arizona, illustrate the versatility of the SIRCUS system.

A. stray light characterization of spectrographs

Spectrographs are spectroradiometers with multi-element array detectors that can acquire an entire spectrum, over some finite spectral region, simultaneously. Spectrographs commonly consist of an entrance port, a dispersing element (such as a grating) to spatially resolve the spectral components of the incident radiation, and mirrors (or lenses) to image the entrance port (often a slit) onto a reference plane where the array detector is located. Because of the dispersing element, the spatial image of the entrance port falls on different regions of the detector array, depending on its wavelength; broadband sources form an image across the entire array. The spectral coverage of a spectrograph is determined by the size of its detector array, the dispersion properties of its grating, and its optical layout. Source spectral distributions can be acquired in a matter of seconds as opposed to minutes often required for conventional, scanned grating systems. The ability to rapidly acquire a spectrum has led to the use of array-based systems in a variety of radiometric, photometric, and colorimetric applications where acquisition speed is an issue, for instance, on a product line, or in cases where the source being measured is not stable over extended periods of time.

In general, we are looking for a solution to the system of equations defined by the measurement equation

$$\vec{S} = \overleftrightarrow{R} \cdot \vec{E}, \tag{5.1}$$

where $\vec{S}$ and $\vec{E}$ are vectors and $\overleftrightarrow{R}$ is a two-dimensional responsivity matrix with non-zero elements corresponding to each element's bandpass function. Several approaches to the solution of the systems of equations have been proposed,[64–68] including solutions that simultaneously correct for both bandpass and stray-light effects[67] and an iterative solution derived from an image reconstruction approach.[68] In the following, we describe the Zong stray light correction algorithm.[63]

In a perfect system, with monochromatic excitation, an image of the entrance slit is formed on the detector array and no light outside of this image is detected. This signal, encompassing several columns on the 2-dimensional detector array or elements in a single channel diode array system, represents the measurand of interest. The detector response to this input is the properly imaged or in-band (IB) signal, S_{IB}.

In a real system, the imaged slit is modified by stray or scattered light (SL) in the system; this scattered radiation can fall on any element in the detector array. In general, the total measured signal consists of both in-band and stray light,

$$\vec{S}_{\text{meas}} = \vec{S}_{\text{IB}} + \vec{S}_{\text{SL}}. \tag{5.2}$$

The scattered light vector, S_{SL}, can be expressed as a fractional part of the in-band signal,

$$\vec{S}_{SL} = \overleftrightarrow{D} \cdot \vec{S}_{IB} + \vec{\delta}. \tag{5.3}$$

The matrix $\overleftrightarrow{D}$ is called the Stray light Distribution Matrix (SDM). $\overleftrightarrow{D}$ fully describes the scattered light characteristics of the system for light within the spectrograph's spectral range, that is, for light whose dominant component is properly imaged onto the array. There is an additional term, δ, in Eq. (5.3) that represents the sum of the detector response to source radiant flux outside the instrument's spectral range, that is, incident flux not imaged onto the detector array. In the following discussion, $\vec{\delta}$ is assumed to be zero. To fill the columns in $\overleftrightarrow{D}$, the responses of the system to monochromatic sources, in our case SIRCUS laser sources, are recorded. For accurate characterization of spectrometers for scattered light, the entrance pupil should be uniformly illuminated by quasi-monochromatic radiation at many wavelengths covering the full spectral range of the incident radiation falling on the focal plane. Typically, a subset of columns is filled using measured values; intermediate column elements are filled by interpolating between measured results. From this characterization, an SDM is formed that fully describes the response of the instrument to scattered light.

Substituting for $\vec{S}_{SL}$, Eq. (5.2) can be expressed as

$$\vec{S}_{\mathrm{meas}} = \vec{S}_{\mathrm{IB}} + \vec{S}_{\mathrm{SL}} = \vec{S}_{\mathrm{IB}} + \overleftrightarrow{D} \cdot \vec{S}_{\mathrm{IB}} = [\overleftrightarrow{I} + \overleftrightarrow{D}] \cdot \vec{S}_{\mathrm{IB}}. \quad (5.4)$$

Finally, solving for $\vec{S}_{IB}$,

$$\vec{S}_{\mathrm{IB}} = [\overleftrightarrow{I} + \overleftrightarrow{D}]^{-1} \cdot \vec{S}_{meas} = \overleftrightarrow{A}^{-1} \cdot \vec{S}_{\mathrm{meas}}, \text{ where } \overleftrightarrow{A} = [\overleftrightarrow{I} + \overleftrightarrow{D}]. \quad (5.5)$$

Equation (5.5) is a system of simultaneous linear equations: each unknown column vector $\vec{S}_{IB}$ can be obtained by directly solving Eq. (5.4) using a proper linear algebraic algorithm (e.g., a Gaussian elimination algorithm). However, in terms of simplicity and calculation speed, it is preferable to solve Eq. (5.5) by inverting matrix $\overleftrightarrow{A}$,

$$\vec{S}_{\mathrm{IB}} = \overleftrightarrow{A}^{-1} \cdot \vec{S}_{\mathrm{meas}} = \overleftrightarrow{C} \cdot \vec{S}_{\mathrm{meas}}. \quad (5.6)$$

$\overleftrightarrow{C}$, the inverse of $\overleftrightarrow{A}$, is the scattered light correction matrix. The development of the matrix $\overleftrightarrow{C}$ is required only once, unless the imaging characteristics of the instrument change. Using Eq. (5.6), the scattered light correction becomes a single matrix multiplication operation.

Figure 32 is a semi-log plot of line spread functions (LSFs) acquired from a spectrograph with excitation wavelengths ranging from 350 nm to 800 nm. Each spectrum is a single image normalized by the peak value. The strong central line in the figure corresponds to the image of the entrance slit formed on the detector array. The broad shoulder, often attributed to a back-reflection from a window that covers the detector array, the second-order diffraction features observed in the top two spectra, and the finite baseline are unwanted signals that degrade a typical measurement. Normalizing the signals by the in-band area and setting the value of the pixels within the in-band area to 0 gives the relative scattered light from those pixels (or from the wavelength of the incident light) into all the other pixels in the detector array.

Based on these measurements, an SDM was created, Fig. 33, and the scattered light correction matrix was developed.[69–72] As an example application of the scattered light correction matrix, Fig. 34 shows the measured signal from a green filter (left) and a green light-emitting diode (LED) (right), on both a logarithmic and expanded linear scale. The black lines are the measured signals and the green lines are the stray light corrected signals. The dashed line represents the 1 Digital Number (DN) level. There should be no light from either artifact at wavelengths less than some cut-on wavelength. Thus, the entire signal from 200 nm to near 425 nm in both measurements arises from stray light in the system. The stray light correction effectively redistributes the counts caused by stray light back to the pixels of the proper wavelength. The stray-light-corrected spectrum reduces the measured signal 2 orders of magnitude or greater in this region, to well below the 1 DN level as shown in Fig. 34. The SLC algorithm has been extended to cover a multiple-input spectrograph system[73] as well as for finite point-spread response

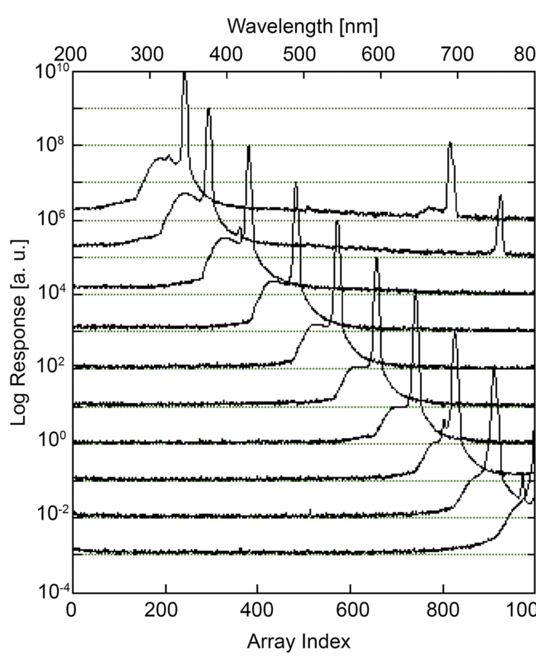

FIG. 32. Semi-log plot of LSF's acquired from a spectrograph with excitation wavelengths ranging from 350 nm to 800 nm. Reprinted with permission from Brown *et al.*, Appl. Opt. **45**, 8218 (2006). Copyright 2006 The Optical Society.

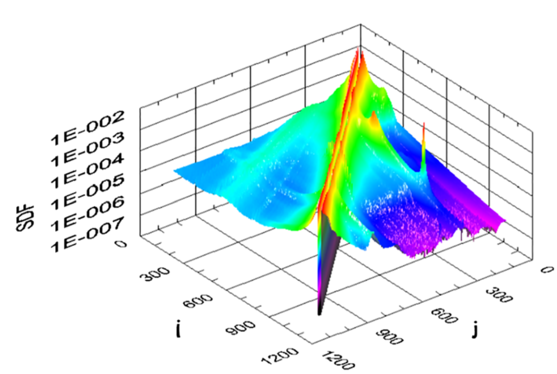

FIG. 33. Stray light distribution matrix (SDM).

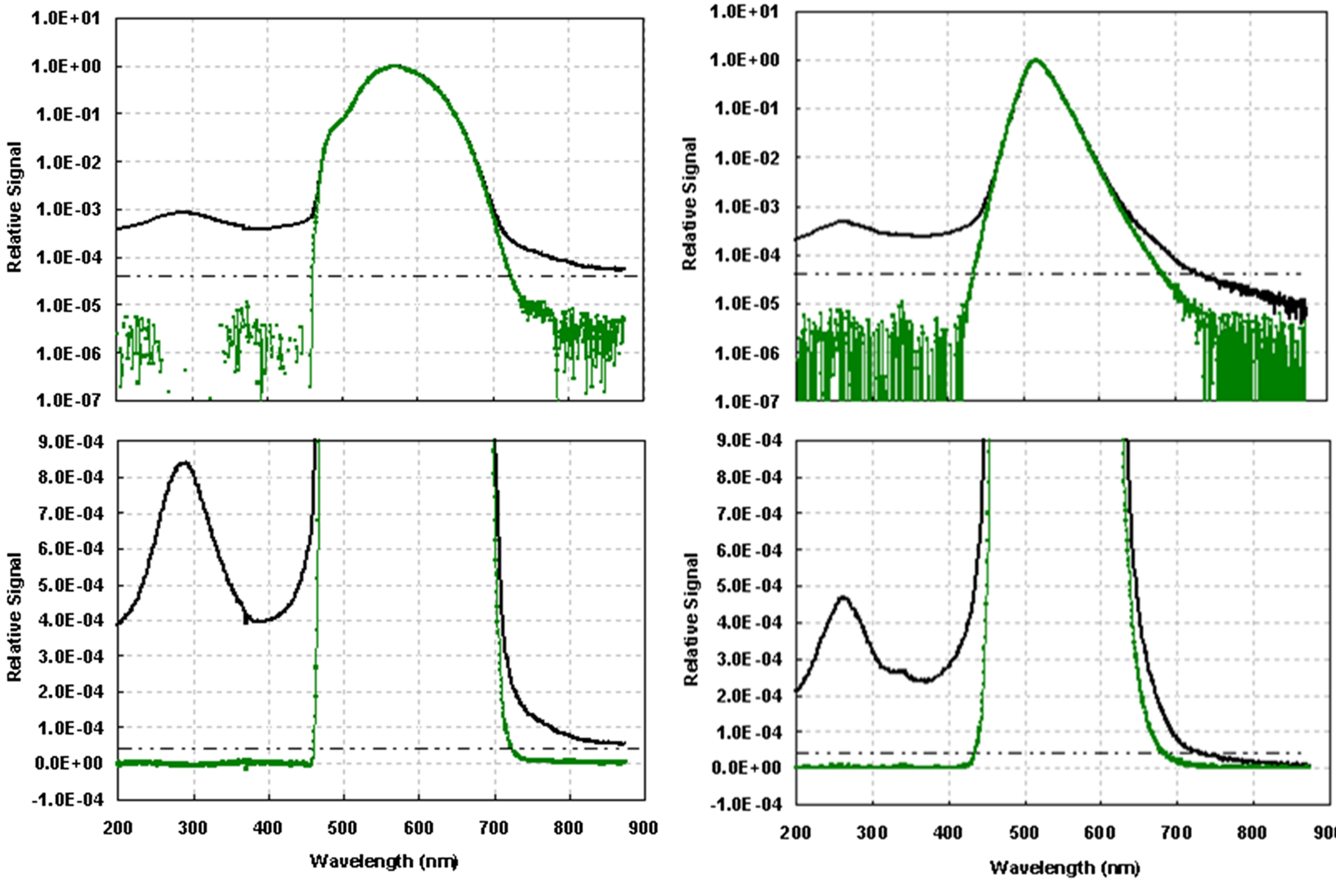

FIG. 34. Stray light correction of a spectrograph's measurements of (left) a green optical filter and (right) a green LED. Original measurement (black); stray light corrected measurement (green). (Top) Logarithmic scale; (bottom) linear scale. The dashed line corresponds to a signal level of 1 DN. Reprinted with permission from Zong *et al.*, Proceedings of the International Commission on Illumination D2, 33–36 (2007). Copyright 2007 CIE.

in imaging systems.[74] The same algorithm can also be used with scanned grating spectroradiometers and monochromators to account for scattered light in these instruments as well.

In the Zong algorithm, the in-band responsivities have effectively been collapsed into single pixels along the diagonal. Measuring the instrument's bandpass function facilitates the development of algorithms that corrects for the finite bandpass of a spectrograph's single pixel responsivity, solving the system of equations defined by Eq. (5.1). Future work is focused on extending the Zong algorithm to account for the finite bandpass of the spectrograph following stray light correction. The approach is to expand the responsivity to include all in-band pixels, typically using SIRCUS characterization measurements and then solve the resulting system of linear equations.

B. Suomi NPP VIIRS sensor calibration

A portable version of the SIRCUS facility, called Traveling SIRCUS (T-SIRCUS), has been utilized for the characterization of NASA and NOAA ground truth instruments, among them the Marine Optical Buoy (MOBY) and the Robotic Lunar Observatory (ROLO);[32] transfer radiometers, e.g., the Visible Transfer Radiometer (VXR);[51,75] and Aerosol Robotic Network (Aeronet) atmospheric and oceanic characterization instruments.[76,77] SIRCUS has also been used to characterize a bread-boarded mockup of the Solar spectral Irradiance Monitor (SIM)[78] and for laboratory characterizations of the Earth Polychromatic Imaging Camera (EPIC),[7] the NIST Advanced Radiometer (NISTAR),[73] the Stratospheric Aerosol and Gas Experiment III (SAGE III) instrument,[71] and the Suomi NPP and Joint Polar Satellite System (JPSS) J1 VIIRS systems,[15] among other instruments. In this section, results of comparing the Suomi NPP VIIRS visible-near-infrared bands absolute spectral responsivity calibration using the standard approach, called the SpMA approach, with the T-SIRCUS approach are presented;[79] end-to-end testing irradiating the solar port using a collimator was also done,[80] but is not discussed here.

T-SIRCUS measurements were made at Ball Aerospace and Technologies Corp. (BATC), while the VIIRS instrument was integrated onto the spacecraft. Results were compared with the vendor calibration. The discussion is limited to VIIRS Bands M01 through M07, extending from 412 nm to 870 nm; bandpasses for these 7 bands, discussed below, are given in Table V. The vendor calibration is a two-step process. In the first step, Band Relative Spectral Responsivities (RSRs) were measured using the instrument vendor's Spectral Measurement Assembly (SpMA), a lamp-monochromator-based approach. For measurements of SpMA by VIIRS, the radiant flux is too low for full aperture illumination and there is a set of transition optics to focus the output of the monochromator onto a single band consisting of 16 detectors at the focal plane. Because

TABLE V. Bandpasses and band-center wavelengths of SUOMI NPP VIIRS Vis-NIR bands M01 through M07. Bandpasses and band-center wavelengths for the IB wavelength ranges of SUOMI NPP VIIRS Vis-NIR bands M01 through M07. All units in nanometers of wavelength.

VIIRS band	SpMA bandwidth	SIRCUS bandwidth	Bandwidth difference SpMA-SIRCUS	SpMA band-center wavelength	SIRCUS band-center wavelength	Band-center wavelength difference SpMA-SIRCUS
M1	18.53	19.15	−0.62	410.84	410.75	0.09
M2	14.02	14.08	−0.06	443.63	443.69	−0.06
M3	18.87	18.80	0.07	486.13	486.34	−0.21
M4	19.82	20.04	−0.22	550.94	550.78	0.16
M5	19.61	19.44	0.17	671.49	671.59	−0.10
M6	14.45	14.36	0.09	745.41	745.59	−0.18
M7	38.74	38.46	0.28	862.00	862.10	−0.10

the incident radiant flux under-fills the instrument's field-of-view, a piece-parts approach must be used to determine the system-level RSR.

In the second step, VIIRS viewed a lamp-illuminated ISS. When combined with the RSRs, the ISS radiances are used to calculate band-average spectral radiances for each of the bands,

$$L^i_{BNDAVG} = \frac{\sum_{\lambda=390}^{\lambda=1000} L_S(\lambda) r^i(\lambda)\,\Delta\lambda}{\sum_{\lambda=390}^{\lambda=1000} r^i(\lambda)\,\Delta\lambda}, \tag{5.7}$$

where $L_S(\lambda)$ is the sphere radiance at wavelength λ and $r^i(\lambda)$ is the relative spectral response of Band i, dimensionless. The net DNs from the instrument measurements of the sphere are divided by these band-averaged spectral radiances to provide band responsivities with units of DN/(W m^{-2} sr^{-1} μm^{-1}).

As discussed in Ref. 79, there are three principal advantages to using the laser-based source approach over the historical SpMA/ISS approach: greater flux, smaller excitation bandpass, and lower wavelength uncertainty. Together, these advantages offer the possibility of calibrating satellite sensor bands with lower uncertainties than is possible using historical calibration approaches. In particular, the greater flux enables the sensor's entrance pupil to be uniformly illuminated by the ISS with radiance levels approaching or exceeding predicted on-orbit radiances.

A SIRCUS-based calibration of SNPP VIIRS was performed at Ball Aerospace and Technologies Corporation (BATC) in Boulder, CO. During SNPP VIIRS testing, the VIIRS sensor was mounted on the SNPP spacecraft with the Earth-view port looking at a 76.2 cm diameter, barium sulfate coated ISS equipped with a 25.4 cm diameter aperture, Fig. 35. The VIIRS telescope was fixed (non-rotating) and VIIRS continuously acquired data. Two calibrated Gershun-tube radiance meters were used at BATC to provide a calibration of two silicon photodiodes mounted on the ISS wall. The calibration related the monitor signal to the sphere radiance. The sphere-mounted photodiodes were calibrated pre- and post-VIIRS measurements in the BATC high bay outside the clean room. During VIIRS measurements of the sphere, the monitor detectors were used to determine the radiance.

The T-SIRCUS tunable laser sources were kept outside the clean room; the output of the lasers was coupled to the ISS using steel-jacketed 200 μm core diameter silica-silica optical fiber. A beamsplitter in the optical path sent a small portion of the laser radiation into a wavemeter that measured the wavelength of the radiation. An electronic shutter in the optical path could be remotely controlled, allowing ambient signal levels to be routinely acquired.

SIRCUS data sets consisted of a timestamp, the laser wavelength, and the monitor signals. The shutter was closed while the wavelength was changed, providing a beginning and end of the wavelength ambient signal in the data streams. These ambient signals combined with timestamps in the data sets facilitated the proper merging of SIRCUS and VIIRS data sets. For NPP VIIRS, the instrument output is in digital numbers (DN). The DNs from the dark periods were subtracted to provide the net DNs for each radiance level from the sphere. The VIIRS net DNs are combined to give an absolute spectral response (ASR), in DN (W m^{-2} sr^{-1})$^{-1}$, for each band at the wavelength measured by the wavemeter.

The ratio between the SIRCUS-based RSRs and the SpMA-based RSRs developed by the NPP Instrument Characterization Support Team (NICST) at NASA's GSFC for Detector 8, VIIRS bands M1 and M7, in the region around

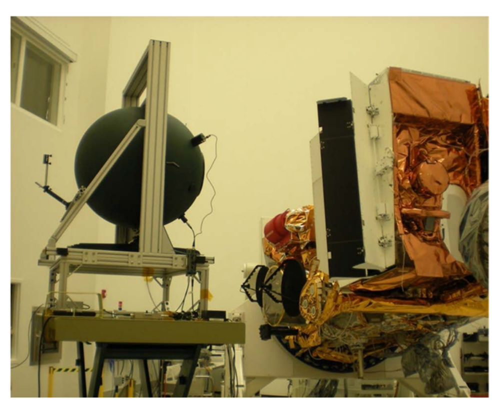

FIG. 35. Experimental setup for SIRCUS laser-based calibration of Suomi NPP VIIRS. The SIRCUS integrating sphere is shown on the left. On the right is the VIIRS instrument with its nadir doors open. The instrument is mounted on the spacecraft bus.

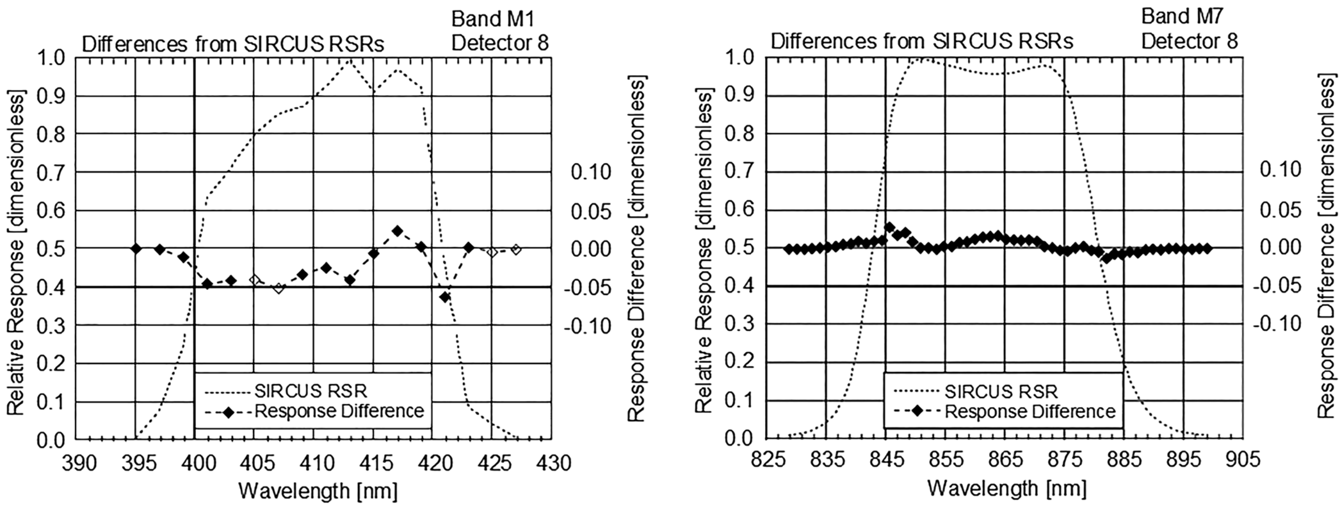

FIG. 36. Ratios between SIRCUS-based RSRs and SpMA-based RSRs over the in-band responsivity of each band. Developed by the NPP Instrument Characterization Support Team at NASA's Goddard Space Flight Center. Reprinted with permission from Barnes *et al.*, Appl. Opt. **54**, 10376–10396 (2015). Copyright 2015 The Optical Society.

the maximum responsivity of each band is shown in Fig. 36. For Band M7, the differences are on the order of 1% to 2%, peaked at the band edges. For Band M1, there is a difference of approximately 5% in the spectral responses on the short wavelength side of the central peak. The differences in the peak-normalized RSRs for Band M1 are readily observable, as shown in Fig. 37. In trying to understand the observed differences in measurements of M1, it is noteworthy that more than one of the SpMA incandescent lamps failed during the spectral measurements by the instrument manufacturer. In some cases, there were no measurements by the SpMA's reference detector before the failure of the lamp. Consequently, there is the possibility of a temporal drift in the output of the SpMA lamp. Since VIIRS and the reference detector measured the output of the SpMA at different times, a drift in the SpMA output could explain the RSR differences observed for Band M1.

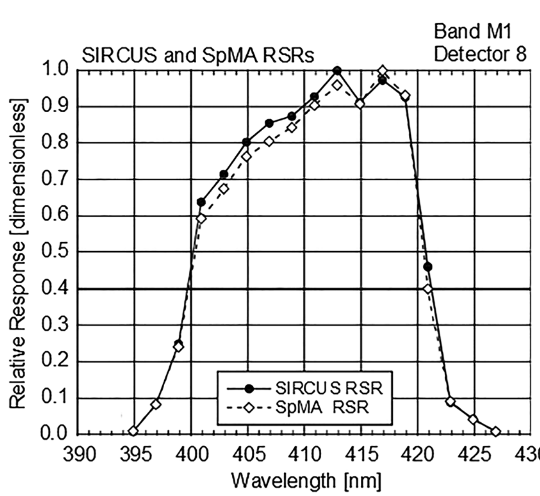

FIG. 37. RSR differences for Band M1 between SIRCUS-based RSRs and SpMA-based RSRs over the in-band responsivity of each band. Developed by the NPP Instrument Characterization Support Team at NASA's Goddard Space Flight Center. Reprinted with permission from Barnes *et al.*, Appl. Opt. **54**, 10376–10396 (2015). Copyright 2015 The Optical Society.

The responsivity for the band is the integration of the monochromatic ASRs in the measurement set. In contrast to the SpMA measurements, the SIRCUS data were not acquired with a constant wavelength spacing; however, it is possible to interpolate the monochromatic ASRs to a set of constant wavelength intervals. This allows band-averaged center wavelengths and bandwidths and band responsivities to be determined. Differences in the band center wavelengths and bandwidths for Detector 8 are given in Table V, while differences in band-averaged responsivities for Detector 8 are given in Table VI. In general, the bandwidths agree at the 1% level, except for band M1, where there is a significant disagreement on the short wavelength side of the central peak. The band responsivities agree within 5%, the target uncertainties in the SpMA measurements.

Each detector in the band has a unique responsivity. Figure 38(a) shows Band M7 detector-to-detector differences in the bandwidth and Fig. 38(b) shows the differences in the centroid wavelength between the two calibration approaches over the 16 detectors in the focal plane. There is a roughly constant difference in the FWHM bandwidth of 0.25 nm, with the SIRCUS bandwidth being smaller. There is a difference

TABLE VI. Differences in band-center wavelengths, bandwidths, and band-averaged responsivities between the SIRCUS-based and the SpMA-based calibration approaches.

VIIRS band	SpMA band responsivity[a]	SIRCUS band responsivity[a]	Responsivity difference (%)
M1	19.392	19.427	−0.18
M2	24.421	23.321	4.72
M3	27.286	26.660	2.35
M4	36.855	35.399	4.11
M5	50.815	49.701	2.24
M6	84.892	84.068	0.98
M7	111.470	110.028	1.31

[a]Units: DN/(W m^{-2} sr^{-1} μm^{-1}).

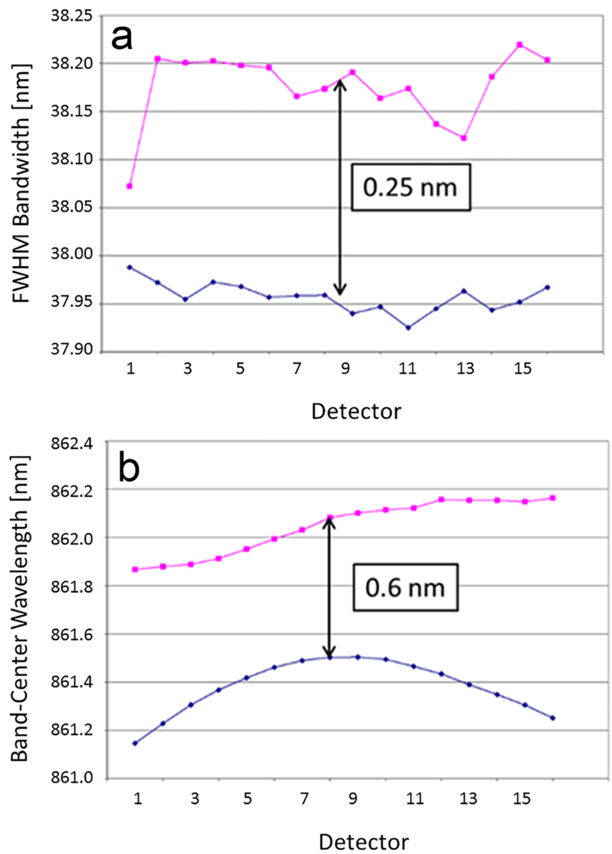

FIG. 38. Detector-to-detector differences in the (a) FWHM bandwidth and (b) band-center wavelength measured using T-SIRCUS and the SpMA. Figures courtesy of David Moyer, The Aerospace Corporation.

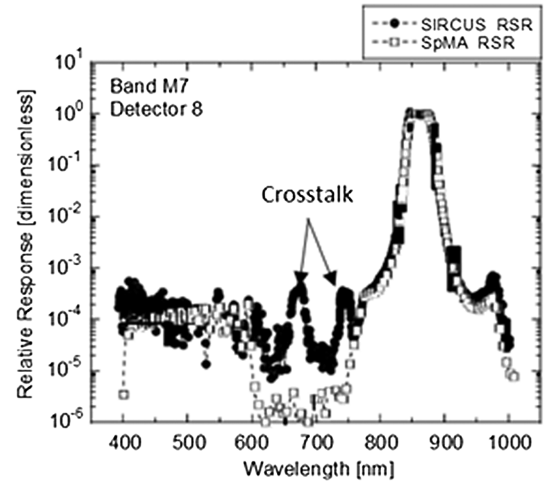

FIG. 39. Total-Band RSRs for band M7. The open squares come from SpMA measurements; the closed circles come from SIRCUS. Channel-to-channel cross talk features are highlighted. Figure courtesy of David Moyer, The Aerospace Corporation.

between the band center wavelength for each detector in the focal plane with the SIRCUS measurements being more symmetric about Detector 8, the center of the focal plane. Finally, there is a detector-dependent offset between the SpMA and the SIRCUS measurements of Band M7 band-center wavelengths. The offset is 0.6 nm for Detector 8.

When excitation in one band causes a signal in a different band, it is called band-to-band cross talk. The optical bandpass filters on the SNPP focal plane showed unexpectedly large scattering, leading to concerns about the quality of the resultant data products. The ocean color community, with very strict uncertainty requirements, was especially concerned that SNPP VIIRS would be "color blind" for their applications, resulting in data products of limited utility.[81] Because the image of the SIRCUS ISS filled the VIIRS focal plane, it was straightforward to look at effects of cross talk on the measurement. Figure 39 shows cross talk from Bands M6 and M5 leading to a non-zero response from Band M7. The signal from Band M7 due to cross talk from Bands M6 and M5 is 4 orders of magnitude lower than the in-band signal. The SIRCUS measurements showed unequivocally that cross talk does not contribute significantly to the measurement error.

The combined standard uncertainty in the SpMA-based calibration of NPP VIIRS, neglecting uncertainties arising from detector-to-detector differences or optical cross talk, is on the order of 2% to 3% for Bands M1–M7, in agreement with historical calibrations using this approach.[82] The dominant uncertainty in this approach is the ISS radiance. Until new primary radiometric standards are developed, there is little chance to significantly reduce this uncertainty. By contrast, the combined standard uncertainty in the SIRCUS-based calibration was 0.5% or lower. *For the first time*, with the SIRCUS calibration of NPP VIIRS, laboratory calibration uncertainties[38] met on-orbit ocean color uncertainty requirements.[83] The measurements resolved community concerns about optical and electronic cross talk[81,84] and gave better RSRs and detector-to-detector variations across the focal plane.[85] For the first time, measurements were made during a full aperture illumination of the solar port; these data were compared with model results and significant differences were observed between the measured and the modeled VIIRS response.[80]

The dominant uncertainty components were detector responsivity and sphere radiance uniformity at the exit port. With additional characterization, these uncertainties can be reduced. The ultimate uncertainty in the sphere radiance over the visible spectral range is less than 0.05%, giving the possibility of a laboratory radiometric calibration uncertainty at the 0.1% level. With these uncertainties, if achieved, laser-based laboratory calibrations would meet the stringent uncertainty requirements for the Climate Absolute Radiance and Refractivity Observatory (CLARREO) Pathfinder Mission in the reflected solar range.[38]

C. Applications to astronomical photometry

Despite the tremendous successes of celestial telescopes, ground-based filter radiometry continues to play an important role in a variety of fields at the forefront of astrophysics, including mapping the expansion history of the universe with type 1a supernovae, determining redshifts to galaxies and clusters, and exploring the properties of dark matter and dark energy.[86,87] Many of these fields require measurement uncertainties on the order of 1%, significantly lower than the current estimated state-of-the art.[88] To achieve measurement uncertainties less than 1%, Stubbs and Tonry[88] have advocated for

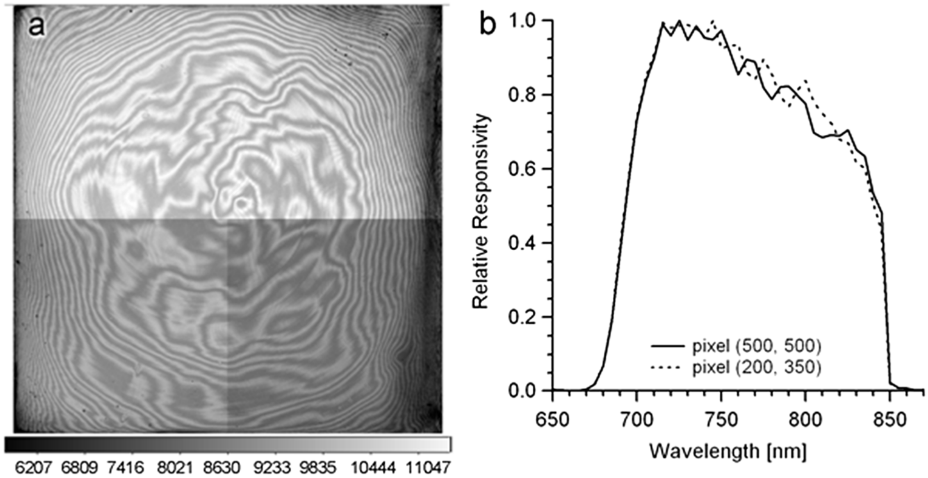

FIG. 40. (a) A KeplerCam image of the flat field screen illuminated with 720 nm light taken with the Sloan i′ filter. (b) A plot of the relative spectral responsivity for two pixels in the top-right quadrant of the CCD showing the unique responsivity of each pixel.

an accurate determination of the atmospheric transmittance and an end-to-end calibration of an astronomical telescope using monochromatic sources, with the scale held on single element silicon detectors traceable to primary standards maintained by NIST. Initial results of the end-to-end calibration of the CTIO mosaic imager and the Blanco telescope using a tunable laser system and a calibrated photodiode were obtained on 20 December 2005.[89]

Several tunable laser-based techniques for improving the precision of observational astronomy were presented by Cramer *et al.*[90] Among other applications, a portable subset of the SIRCUS lasers has been used for *in situ* system-level measurements of the relative spectral response of the PanSTARRS telescope/Gigapixel imager on Haleakala, HI[86] and the KeplerCam on the 1.2 m telescope at the Fred Lawrence Whipple Observatory in southern Arizona.[90,91] System-level measurements of PanSTARRS showed a radial spatial variation in filter passband. In addition, fringing was observed in the image at the focal plane. At ∼900 nm, the peak-to-peak fringe amplitude was approximately 5%.

For the characterization of the KeplerCam filter bands, the flat field screen in the telescope dome was illuminated with laser light coupled through an optical fiber and uniformly dispersed with an engineered diffuser. Figure 40 shows fringing in a KeplerCam image (using the Sloan i′ filter) of the flat field screen illuminated with 720 nm light. A comparison of two pixels shows a significant difference in the relative spectral responsivity across the filter band.

VI. CONCLUSIONS

The availability of tunable lasers defines the spectral coverage possible in SIRCUS, while the quality of the reference standard detectors and their uncertainties ultimately establish the calibration uncertainties achievable. The flux available on SIRCUS, 5 to 6 orders of magnitude greater than available flux from conventional lamp-monochromator systems, expands the capability of calibration services. Among other applications, full illumination of large aperture sensors became feasible, enabling Earth remote sensing sensors such as VIIRS and astronomical telescopes such as PanSTARRS to be characterized and calibrated.[86] The available flux led to the accurate characterization of stray light in spectrographs and the subsequent development of a stray light correction algorithm and a bandpass correction algorithm applicable to spectrographs and scanning monochromator/spectrometer systems. The low uncertainties achieved on the Si tunnel trap detectors open up a new approach to the determination of temperature above the melting point of gold,[57] realization of the SI base unit, candela, with a significantly lower uncertainty, and can lead to the calibration of photometers and colorimeters with lower uncertainties than previously possible.[92]

Advances in the radiometric characterization and calibration of irradiance and radiance meters offered by laser-based calibration approaches have motivated the adoption of the approach by a number of national metrology institutions (NMIs), primary standards laboratory laboratories, and instrument vendors. NMIs with laser-based calibration facilities include the National Physical Laboratory, Great Britain (NPL);[35] the Physikalisch-Technische Bundesanstalt, Germany (PTB);[93] the Centre for Metrology and Accreditation, Finland (MIKES);[94] the Commonwealth Scientific and Industrial Research Organization, Australia;[95] the Chinese Academy of Sciences, China,[96] and Korea.[97] Within the U.S., the National Aeronautics and Space Administration's (NASA's) Goddard Space Flight Center has developed the Goddard Laser for Absolute Measurements of Radiance (GLAMR),[98] a laser-based calibration facility for the characterization of relatively large aperture aircraft and satellite sensors;[99] in addition, Goddard has joined with the University of Boulder's Laboratory for Atmospheric and Space Physics (LASP) in the development of the Sun-Climate Research Center. Critical to the success of the Center is a Spectral Radiometer Facility (SRF) that uses a SIRCUS tunable laser system (SRF_SIRCUS) to provide irradiance levels comparable to solar irradiance over the spectral range from 210 nm to 2400 nm.[100] Finally, companies using tunable lasers for characterization and calibration of their products include Gigahertz Optik and Instrument Systems/Konika Minolta.

Advances in tunable laser systems over the past decade have greatly reduced their cost and simplified their operation. However, the acquisition and maintenance of lasers sufficient to cover broad wavelength ranges can be cost prohibitive. Consequently, alternative approaches are being considered to generate the incident flux used for calibrations, for example, supercontinuum source-monochromator systems.[101,102] Currently, in SIRCUS, an ACR is being configured to make low uncertainty irradiance measurements with the goal of calibrating transfer standard irradiance meters against an ACR directly in irradiance mode; a supercontinuum source-pumped Laser Line Tunable Filter (LLTF) and a kHz OPO system are being evaluated as possible replacements for the tunable laser systems; and low Noise Equivalent Power (NEP) pyroelectric detectors are being evaluated as candidate working standard detectors[103] whose responsivity in the SWIR can be derived from measurements in the visible-near infrared spectral range against primary standard Si-based detector, greatly simplifying the derivation and maintenance of an SI-traceable radiance responsivity in the 1.6 μm to 2.5 μm range.

ACKNOWLEDGMENTS

The authors would like to recognize John Grangaard, USAF (ret.) for his early and continued support for the development of the SIRCUS facility; Dennis K. Clark, NOAA (dec.) for his contributions to the development of the stray light correction algorithm for spectrographs; and Bruce Guenther (NOAA and Stellar Solutions) for advocating and leading the laser-based characterization and calibration efforts of SNPP VIIRS.

[1]S. W. Brown, G. Eppeldauer, and K. R. Lykke, "Facility for spectral irradiance and radiance responsivity calibrations using uniform sources," Appl. Opt. **45**(32), 8218–8237 (2006).
[2]J. M. Houston and J. P. Rice, "NIST reference cryogenic radiometer designed for versatile performance," Metrologia **43**, S31–S35 (2006).
[3]J. Fowler and M. Litorja, "Geometric area measurements of circular apertures for radiometry at NIST," Metrologia **40**, S9–S12 (2003).
[4]Rippey Corporation, El Dorado Hills, CA.
[5]P.-S. Shaw *et al.*, "Ultraviolet characterization of integrating spheres," Appl. Opt. **46**, 5119–5128 (2007).
[6]P.-S. Shaw, U. Arp, and K. R. Lykke, "Measurement of He ultraviolet-induced fluorescence yield from integrating spheres," Metrologia **46**, S191–S196 (2009).
[7]E. A. Early *et al.*, "Radiometric calibration of the scripps Earth polychromatic imaging Camera," Proc. SPIE **4483**, 77–84 (2001).
[8]T. Stone, U.S. Geological Survey, Flagstaff, AZ, personal communication (2005).
[9]P.-S. Shaw *et al.*, *National Institute of Standards and Technology Primary Optical Watt Radiometer* (unpublished).
[10]N. P. Fox, "Trap detectors and their properties," Metrologia **28**, 197–202 (1991).
[11]E. F. Zalewski and C. R. Duda, "Silicon photodiode device with 100% external quantum efficiency," Appl. Opt. **22**(18), 2867–2873 (1983).
[12]T. R. Gentile *et al.*, "Internal quantum efficiency modeling of silicon photodiodes," Appl. Opt. **49**(10), 1859–1864 (2010).
[13]P.-S. Shaw, R. Gupta, and K. R. Lykke, "Stability of photodiodes under irradiation with a 157-nm pulsed excimer laser," Appl. Opt. **44**, 197–207 (2005).
[14]G. P. Eppeldauer and D. C. Lynch, "Opto-mechanical and electronic design of a tunnel-trap Si-radiometer," J. Res. Natl. Inst. Stands. Technol. **105**, 813–828 (2000).
[15]G. P. Eppeldauer and V. B. Podobedov, "Infrared spectral responsivity scale realization and validations," Appl. Opt. **51**, 6003–6008 (2012).
[16]General Photonics Corp., Chino, CA.
[17]Coherent Nufern, East Granby, CT; NuBeam Flat-Top.
[18]E. F. Zalewski, "Radiometry and photometry," in *Handbook of Optics*, edited by M. Bass (McGraw-Hill, Inc., New York, 1995), pp. 17–24.
[19]P. Moon and D. E. Spencer, "Radiant flux through apertures-I," J. Franklin Inst. **306**(1), 1 (1978).
[20]Lockheed Martin, Bethesda, MD; Argos Aculight.
[21]Daylight Solutions Inc., San Diego, CA.
[22]A. Robertson and A. I. Ferguson, "Synchronously pumped all-solid-state lithium triborate optical parametric oscillator in a ring configuration," Opt. Lett. **19**, 117–119 (1994).
[23]S. D. Butterworth, S. Girard, and D. C. Hanna, "High-power, broadly tunable all-solid-state synchronously pumped lighium triborate optical parametric oscillator," J. Opt. Soc. Am. B **12**(11), 2158–2167 (1995).
[24]T. W. Tukker, C. Otto, and J. Greve, "Design, optimization and characterization of a narrow-bandwidth optical parametric oscillator," J. Opt. Soc. Am. B **16**(1), 90–95 (1999).
[25]F. Kienle *et al.*, "High-power, high repetition-rate, green-pumped, picosecond LBO optical parametric oscillator," Opt. Express **20**(7), 7008–7014 (2012).
[26]M. Jurna *et al.*, "Noncritical, phase-matched lithium triborate optical parametric oscillator for high resolution coherent anti-Stokes Raman scattering spectroscopy and microscopy," Appl. Phys. Lett. **89**, 251116 (2006).
[27]M. Tsunekane *et al.*, "Broadband tuning of a continuous-wave doubly resonant, lithium triborate, optical parametric oscillator from 791 to 1620 nm," Appl. Opt. **37**(27), 6459–6462 (1998).
[28]Coherent, Inc., Santa Clara, CA; Paladin Advanced 532.
[29]M. H. Dunn and A. I. Ferguson, "Coma compensation in off-axis laser resonators," Opt. Commun. **20**(2), 214–219 (1977).
[30]C. Du *et al.*, "Efficient intracavity second-harmonic generation at 1.06 μm in a BiB_3O6 (BIBO) crystal," Appl. Phys. B **73**(3), 215–217 (2001).
[31]Ekspla, Lituania; NT242.
[32]Y. Zong *et al.*, "A new method for spectral irradiance and radiance responsivity calibrations using kilohertz pulsed tunable optical parametric oscillators," Metrologia **49**, S124–S129 (2012).
[33]K. D. Mielenz, R. D. Saunders, and J. B. Shumaker, "Spectroradiometric determination of the freezing temperature of gold," J. Res. Natl. Inst. Stands. Technol. **95**, 49–67 (1990).
[34]D. J. Pugh and K. Jackson, "Automatic gauge block measurement using multiple wavelength interferometry," Proc. SPIE **656**, 244–250 (1986).
[35]V. E. Anderson, N. P. Fox, and D. H. Nettleton, "Highly stable, monochromatic and tunable optical radiation source and its application to high accuracy spectrophotometry," Appl. Opt. **31**(4), 536–545 (1992).
[36]L. Yan *et al.*, "Improved beam uniformity in multimode fibers using piezoelectric-based spatial mode scrambling for medical applications," Opt. Eng. Lett. **47**, 090502-1–090502-3 (2008).
[37]Y. Fujimaki and H. Taniguchi, "Reduction of speckle contrast in multimode fibers using piezoelectric vibrator," Proc. SPIE **8960**, 89601S (2014).
[38]D. Dayton, H. Gonglewski, and C. StArnauld, "Laser speckle and atmospheric scintillation dependence on laser spectral bandwidth," Proc. SPIE **7476**, 74760A (2009).
[39]See http://www.nist.gov/traceability/ for NIST policy on traceability.
[40]J. M. Houston and D. J. Livigni, "Comparison of two cryogenic radiometers at NIST," J. Res. Natl. Inst. Stand. Technol. **106**, 641–647 (2001).
[41]J. Geist, E. F. Zalewski, and A. R. Schaefer, "Spectral response self-calibration and interpolation of silicon photodiodes," Appl. Opt. **19**(22), 3795–3799 (1980).
[42]E. F. Zalewski and J. Geist, "Silicon photodiode absolute spectral response self-calibration," Appl. Opt. **19**(8), 1214–1216 (1980).
[43]J. L. Gardner, "Uncertainty propagation for NIST visible spectral standards," J. Res. Natl. Inst. Stand. Technol. **109**, 305–318 (2004).
[44]J. L. Gardner, "Uncertainties in interpolated spectral data," J. Res. Natl. Inst. Stand. Technol. **108**(1), 69–78 (2003).
[45]T. C. Larason and J. M. Houston, *Spectroradiometric Detector Measurements: Ultraviolet, Visible, and Near-Infrared Detectors for Spectral Power*, NIST Special Publication 250-41 (U.S. Department of Commerce, NIST, Gaithersburg, MD, 2008).
[46]T. R. Gentile *et al.*, "National institute of standards and technology high-accuracy cryogenic radiometer," Appl. Opt. **35**(7), 1056–1068 (1996).
[47]T. R. Gentile, J. M. Houston, and C. L. Cromer, "Realization of a scale of absolute spectral response using the NIST high-accuracy cryogenic radiometer," Appl. Opt. **35**(22), 4392–4403 (1996).
[48]T. C. Larason, S. S. Bruce, and C. L. Cromer, "The NIST high accuracy scale for absolute spectral response from 406 nm to 920 nm," J. Res. Natl. Inst. Stand. Technol. **101**, 133–140 (1996).
[49]J. H. Walker *et al.*, *Spectral Irradiance Calibrations*, NBS Special Publication 250-20 (U.S. Government Printing Office, Washington, DC, 1987).

[50]S. W. Brown and B. C. Johnson, "Development of a portable integrating sphere source for the Earth observing system's calibration validation programme," Int. J. Remote Sensing **24**, 215–224 (2002).

[51]B. C. Johnson *et al.*, "Comparison of cryogenic radiometry and thermal radiometry calibrations at NIST using multichannel filter radiometers," Metrologia **40**, S216–S219 (2003).

[52]J. Fischer and J. Ullrich, "The new system of units," Nat. Phys. **12**, 4–7 (2016).

[53]E. R. Woolliams *et al.*, "Primary radiometry for the Mise-en-Pratique for the definition of the Kelvin: The hyprid method," Int. J. Thermophys. **32**(11), 1–11 (2011).

[54]H. Preston-Thomas, "The international temperature scale of 1990 (ITS-90)," Metrologia **27**, 3–10 (1990).

[55]D. Halliday and R. Resnick, *Fundamentals of Physics*, 2nd ed. (John Wiley and Sons, Inc., New York, 1981).

[56]H. W. Yoon *et al.*, "The realization and the dissemination of the detector-based Kelvin," in Proceedings of Tempmeko 04, Dubrovnik, Croatia, 2004.

[57]H. W. Yoon *et al.*, "Thermodynamic radiation thermometry for the next SI," Int. J. Thermophys. **29**(1), 285–300 (2008).

[58]H. W. Yoon, "The realization and the dissemination of thermodynamic temperature scales," Metrologia **43**, S22–S26 (2006).

[59]H. W. Yoon *et al.*, "Temperature scales using radiation thermometers calibrated from absolute irradiance and radiance responsivity," in NCSL International Workshop and Symposium, Orlando, FL, 2003.

[60]N. P. Fox, J. E. Martin, and D. H. Nettleton, "Absolute spectral radiometric determination of the thermodynamic temperatures of the melting/freezing points of gold, silver, and aluminium," Metrologia **28**, 357–374 (1991).

[61]H. W. Yoon and C. E. Gibson, "Determination of radiance temperatures using detectors calibrated for absolute spectral power response," in Proceedings of the 7th International Symposium on Temperature and Thermal measurements in Industry and Science (TEMPMEKO '99), edited by J. F. Dubbeldam (Delft, The Netherlands, 2000), pp. 737–742.

[62]H. W. Yoon *et al.*, "Thermodynamic radiation thermometry using radiometers calibrated for radiance responsivity," Int. J. Thermophys. **32**, 2217 (2011).

[63]K. Anhalt and G. Machin, "Thermodynamic termperature by primary radiometry," Philos. Trans. R. Soc. A **374**, 20150041 (2016).

[64]E. I. Stearns and R. E. Stearns, "An example of a method for correcting radiance data for bandpass error," Color Res. Appl. **13**(4), 257–259 (1988).

[65]J. L. Gardner, "Spectral deconvolution applications for colorimetry," Color Res. Appl. **39**(5), 430–435 (2013).

[66]Y. Ohno, "A flexible bandpass correction method for spectrometers," in AIC Color 05-10th Congress of the International Colour Association, Grenada, Spain, 2005.

[67]S. Nevas *et al.*, "Simultaneous correction of bandpass and stray-light effects in array spectroradiometer data," Metrologia **49**, S43–S47 (2012).

[68]S. Eichstaedt *et al.*, "Comparison of the Richardson-Lucy method and a classical approach for spectrometer bandpass correction," Metrologia **50**, 107–118 (2013).

[69]S. W. Brown *et al.*, "Stray-light correction algorithm for spectrographs," Metrologia **40**, S81–S84 (2003).

[70]S. W. Brown *et al.*, "Advances in Radiometry for Ocean Color," in *Ocean Optics Protocols for Satellite Ocean Color Sensor Validation*, Volume VI of Special Topics in Ocean Optics Protocols and Appendices, Revision 4, edited by J. L. Mueller, G. S. Fargion, and C. R. McClain (NASA, Greenbelt, MD, 2004), pp. 8–35.

[71]M. A. Feinholz *et al.*, "Stray light correction of the marine optical system," J. Atmos. Oceanic Technol. **26**, 57–73 (2009).

[72]Y. Zong *et al.*, "A simple spectral stray light correction method for array spectroradiometers," Appl. Opt. **45**(6), 1111–1119 (2006).

[73]M. A. Feinholz *et al.*, "Stray light correction algorithm for multichannel hyperspectral spectrographs," Appl. Opt. **51**(16), 3631–3641 (2012).

[74]Y. Zong *et al.*, "Correction of stray light in spectroradiometers and imaging instruments," in Proceedings of the CIE 26th Session (CIE, Beijing, China, 2007), Vol. D2, pp. 33–36.

[75]B. C. Johnson *et al.*, "System-level calibration of a transfer radiometer used to validate EOS radiance scales," Int. J. Remote Sensing **24**, 339–356 (2003).

[76]N. Souaidia *et al.*, "Comparison of laser-based and conventional calibrations of sun photometers," Proc. SPIE **5155**, 61–72.

[77]B. C. Johnson *et al.*, "Calibration and characterization of a SeaPRISM radiometer for AERONET-OC," available at: https://www.eposters.net/poster/calibration-and-characterization-of-a-seaprism-radiometer-for-aeronet-oc.

[78]J. W. Harder *et al.*, "The SORCE SIM solar spectrum: Comparison with recent observations," Solar Phys. **263**, 3–24 (2010).

[79]R. A. Barnes *et al.*, "Comparison of two methodologies for calibrating satellite instruments in the visible and near-infrared," Appl. Opt. **54**(35), 10376–10396 (2015).

[80]J. McIntire *et al.*, "Results from solar reflective band end-to-end testing for VIIRS F1 sensor using T-SIRCUS," Proc. SPIE **8153**, 8153OI (2011).

[81]E. Kintisch, "U. S prepares to launch flawed satellite," Science **319**, 886 (2008).

[82]J. J. Butler and R. A. Barnes, "Calibration strategy for the Earth observing system (EOS)-AM1 platform," IEEE Trans. Geosci. Remote Sensing **36**(4), 1056–1061 (1998).

[83]H. R. Gordon, "The Marine Optical Muoy (MOBY) radiometric calibration and uncertainty budget for ocean color satellite sensor vicarious calibration," Proc. SPIE **6744**, 67441M1–67441M6 (2007).

[84]See http://oceancolor.gsfc.nasa.gov/DOCS/ocb.oceancolorletter.pdf for D. A. Siegel, J. A. Yoder, and C. R. McClain, Thoughts about the future of satellite ocean color observations, 2008.

[85]B. Guenther, "Application of laser-source-based calibration for VIIRS for ultra-high accuracy spectroradiometric calibrations," Proc. SPIE **8372**, 8372OE (2012).

[86]C. W. Stubbs *et al.*, "Precise throughut determination of the PanSTARRS telescope and the gigapixel imager using a calibrated silicon photodiode and a tunable laser: Initial results," Astrophys. J. Suppl. Series **191**, 376–388 (2010).

[87]P. M. Korngut *et al.*, "The cosmic infrared background experiment (CIBER): The narrowband spectrometer," Astrophys. J. Suppl. Series **207**(34), 1–12 (2013).

[88]C. W. Stubbs and J. L. Tonry, "Toward 1% photometry: End-to-end calibration of astronomical telescopes and detectors," Astrophys. J. **646**, 1436–1444 (2006).

[89]C. W. Stubbs *et al.*, "Preliminary results from detector-based throughput calibration of the CTIO mosaic imager and Blanco telescope using a tunable laser," in *The Future of Photometric, Spectrophotometric and Polarimetric Standardization*, ASP Conference Series Vol. 364, edited by C. Sterken (Astronomical Society of the Pacific, San Francisco, 2007).

[90]C. E. Cramer *et al.*, "Tunable laser techniques for improving the precision of observational astronomy," Proc. SPIE **8450**, 8450OS (2012).

[91]J. T. Woodward *et al.*, "Spectroradiometric calibration of telescopes using laser illumination of flat field screens," Proc. SPIE **7737**, 77372A (2010).

[92]G. P. Eppeldauer, "Spectral responsivity-based calibration of photometer and colorimeter standards," J. Mod. Opt. **60**, 1124 (2013).

[93]A. Sperling, Physikalisch Technische Bundesanstalt, Braunschweig, Germany, personal communication (2002).

[94]M. Noorma *et al.*, "Characterization of filter radiometers with a wavelength-tunable laser source," Metrologia **40**, S220–S223 (2003).

[95]J. L. Gardner *et al.*, "New basis for the Australian realization of the candela," Metrologia **35**, 235–239 (1998).

[96]P. Zou *et al.*, "Absolute spectral radiance responsivity calibration of the radiance transfer standard detector," Proc. SPIE **6621**, 66211B (2008).

[97]D.-H. Lee *et al.*, "The KRISS PLUS (Pulsed Laser-based Uniform Source) facility for measurement of spectral radiance responsivity," in XX IMEKO World Congress, Busan, Republic of Korea, 2012.

[98]See http://neptune.gsfc.nasa.gov/uploads/files/618_2015_04_rh_mccorkel.pdf for McCorkel, GLAMR.

[99]A. Angal *et al.*, "Radiometric Calibration of G-LiHT's imaging spectrometer using GLAMR for satellite sensor intercalibration," Proc. SPIE **9607**, 9607c (2015).

[100]See http://lasp.colorado.edu/home/scrc/facilities/engineering-division/facilities/spectral-radiometer-facility/ for information about the LASP Spectral Radiometer Facility.

[101]J. T. Woodward *et al.*, "Supercontinuum sources for metrology," Metrologia **46**, S277–S282 (2009).

[102]A. P. Levick *et al.*, "Spectral radiance source based on supercontinuum laser and wavelength tunable bandpass filter: The spectrally tunable absolute irradiance and radiance source," Appl. Opt. **53**(16), 3508–3519 (2014).

[103]G. Eppeldauer *et al.*, "Extension of the NIST spectral responsivity scale to the infrared using improved-NEP pyroelectric detectors," Metrologia **46**, S155–S159 (2009).

[104]Identification of commercial equipment to specify adequately an experimental problem does not imply recommendation or endorsement by the NIST nor does it imply that the equipment identified is necessarily the best available for the purpose.